Supplementary Information

Cost-effective interfacial high-concentration electrolyte for stable lithium metal batteries

Wenya Wu[1#], Tingting Li[1#], Tuo Zhao[1], Rui Qiao[1], Yong Li[2], Shengjie Chen[1], Zirui Jiang[1], Sai Zhang[1], Caiwang Mao[1], Junkai Deng[1], Jiangxuan Song[1]*

[1]State Key Laboratory for Mechanical Behavior of Materials, Shaanxi International Research Center for Soft Matter, Xi'an Jiaotong University, Xi'an 710049, China

[2]State Key Laboratory of Space Power-Sources Technology, Shanghai Institute of Space Power Sources, Shanghai 200245, China

[#]These authors contributed equally

*Corresponding author. Email: songjx@xjtu.edu.cn

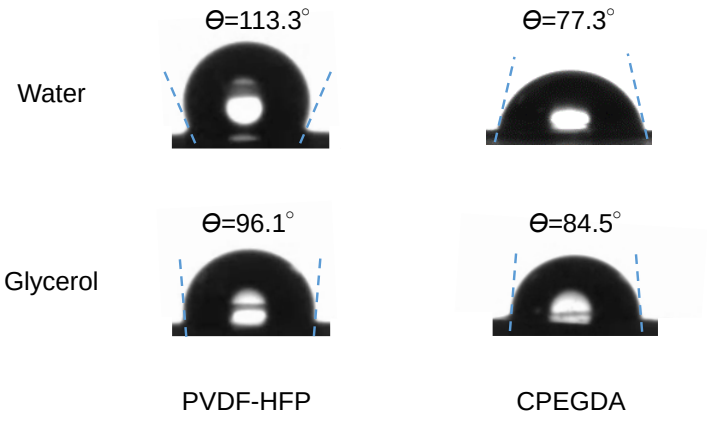

Supplementary Fig. 1. **Surface wettability characterization**. Contact angle measurements of pure PVDF-HFP and CPEGDA films using deionized water and glycerol as wetting liquids.

Supplementary Note 1:

The Flory-Huggins interaction parameter between PVDF-HFP (i) and CPEGDA (j) was calculated by the following Equation (1):

$$\chi_{ij} = \frac{V_0}{RT}\left(\delta_i - \delta_j\right)^2 \quad (1)$$

δ was calculated by the Equation (2):

$$\delta = \frac{K}{\sqrt{\gamma_s}} \quad (2)$$

Where K (116×10^3 $m^{-1/2}$) is the proportionality constant, V_0 is the geometric mean of the polymer segment molar volume, R is the gas constant, and T is the absolute temperature. Υ_s is the surface tension, which is composed of the dispersion force γ_s^D and the polarization force γ_s^P. The surface energy can be calculated by the Owens and Wendt Equation (Equation (3)):

$$(1+\cos\Theta)\gamma_1 = 2(\gamma_s^D)^{\frac{1}{2}}(\gamma_l^D)^{\frac{1}{2}} + 2(\gamma_s^P)^{\frac{1}{2}}(\gamma_l^P)^{\frac{1}{2}} \quad (3)$$

Where Θ is the contact angle of two probe liquids (deionized water and glycerol) on the substrate (PVDF-HFP and CPEGDA films), as shown in Supplementary Fig. 1, measured by contact angle measurements through DSA 30. Υ_l is the surface energy of the testing liquid, which is composed of the dispersion force γ_l^D and the polarization force γ_l^P. For water, the values of Υ_l, γ_l^D and γ_l^P are 72.8, 21.8, and 51.0 mJ m^{-2}, respectively. For glycerol, the corresponding values are 63.4, 37.0, and 26.4 mJ m^{-2},

respectively. The above parameters and Flory-Huggins interaction parameters (χ = 6.5 k) calculated according to Equations (1)-(3), were summarized in Supplementary Table 1.

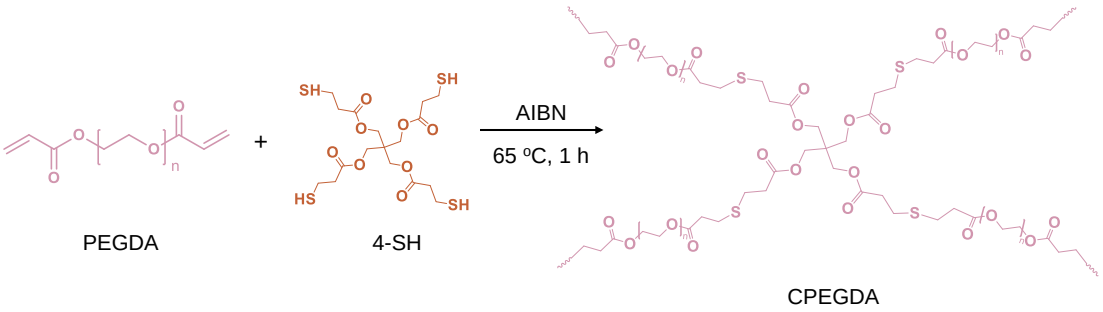

Supplementary Fig. 2. **Synthesis of CPEGDA**. CPEGDA was synthesized by reacting PEGDA, 4-SH crosslinker, and AIBN in an oil bath at 65 °C for 1 h.

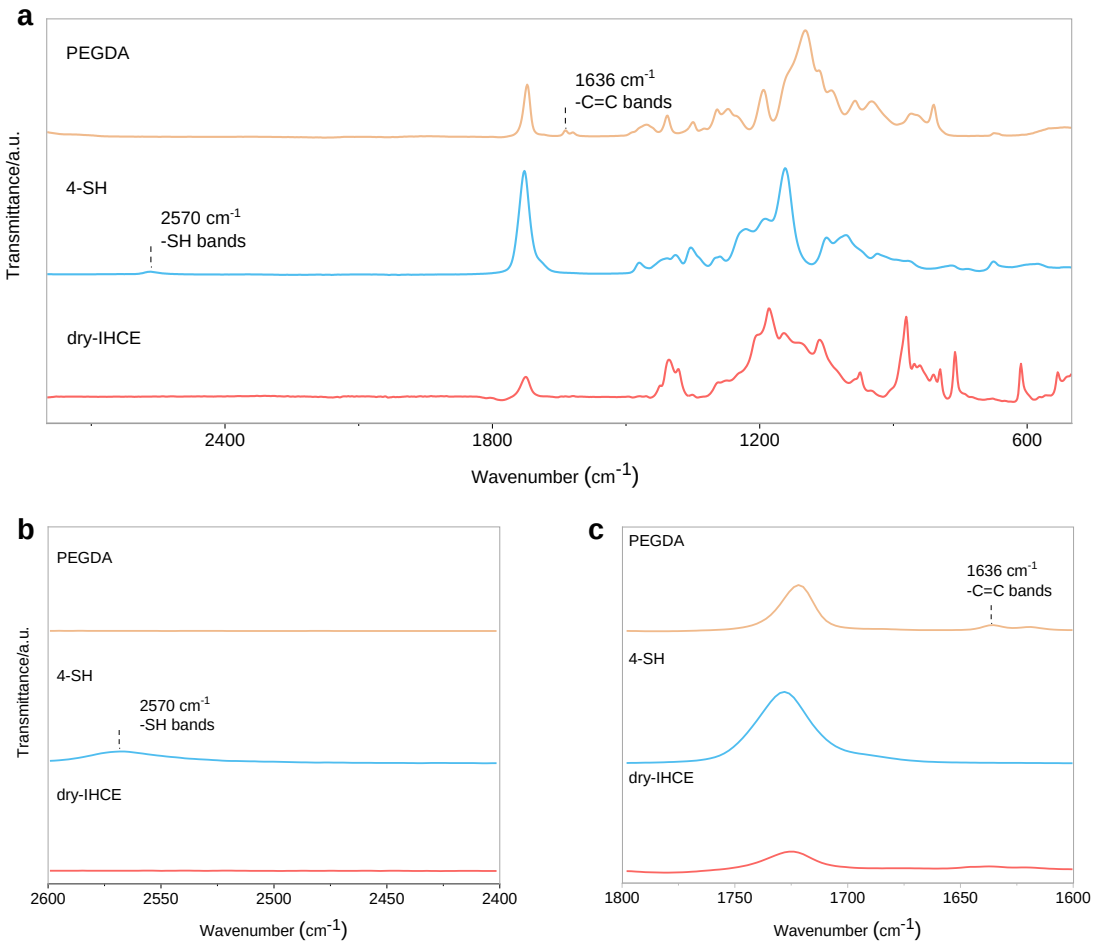

Supplementary Fig. 3. **FTIR spectra of pure PEGDA, 4-SH, and synthesized IHCE**. a, Full spectra in the range of 2800-500 cm^{-1}. b, Enlarged spectra from 2600 cm^{-1} to 2400 cm^{-1}. c, Enlarged spectra from 1800 cm^{-1} to 1600 cm^{-1}. As shown in Supplementary Fig. 3b, c, the characteristic peaks of PEGDA (-C=C) at 1636 cm^{-1} and 4-SH (-SH) at 2570 cm^{-1} disappeared after polymerization, confirming the successful formation of IHCE.

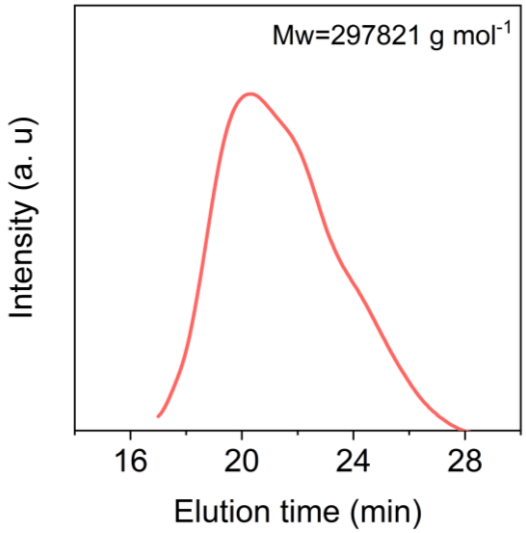

Supplementary Fig. 4. **GPC spectrum of IHCE**. (M_w = 297, 821 g mol^{-1}, PDI 3.54)

Supplementary Note 2:

The FTIR spectra in Supplementary Fig. 3 illustrate the chemical transformation during the synthesis of IHCE. Specifically, the characteristic absorption peak of the C=C bond in pure PEGDA at 1636 cm^{-1} and the S-H stretching vibration of 4-SH at 2570 cm^{-1} are observed in the spectra of the raw materials. After polymerization, both of these peaks disappear, indicating the successful reaction of the C=C groups in PEGDA and the S-H group in 4-SH via a "click reaction", resulting in the formation of a crosslinked polymer network.

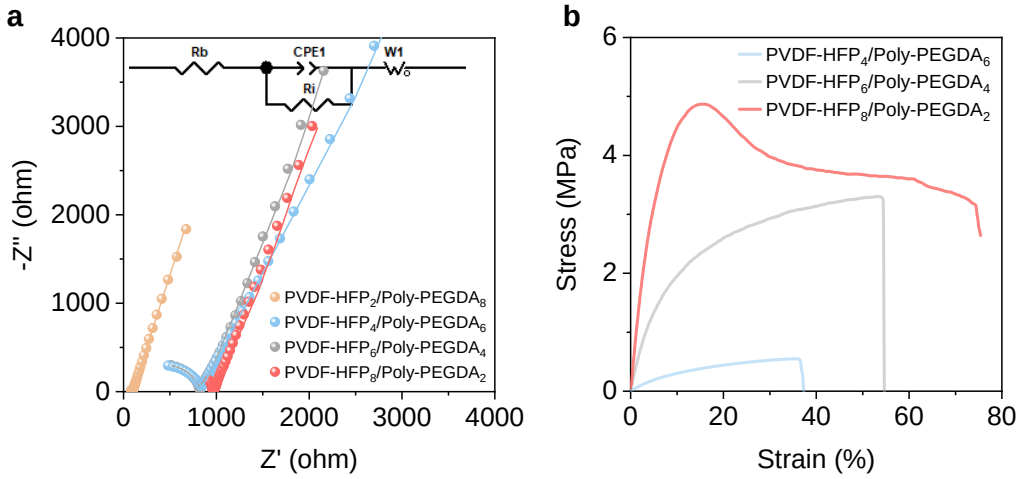

Supplementary Fig. 5. **Ratio optimization of PVDF-HFP$_m$/CPEGDA$_n$**. a, Nyquist plots of the PVDF-HFP$_m$/CPEGDA$_n$ membranes for ionic conductivity measured at 25 °C. b, Stress-strain curves of the PVDF-HFP$_m$/CPEGDA$_n$ membranes at 25 °C.

Supplementary Note 3:

The ionic conductivities of PVDF-HFP$_m$/CPEGDA$_n$ membranes were evaluated using symmetric SS||SS cells by electrochemical impedance spectroscopy (EIS) tests. The measured parameters are summarized in Supplementary Table 2. The ionic conductivities (σ) were calculated using Equation (4):"

$$\sigma = \frac{L}{R_b S} \tag{4}$$

where σ is the ionic conductivity, L is the membrane thickness, S is the electrode area, and R_b is the bulk resistance obtained by AC impedance (the fitting error of R_b is 0.311%)."

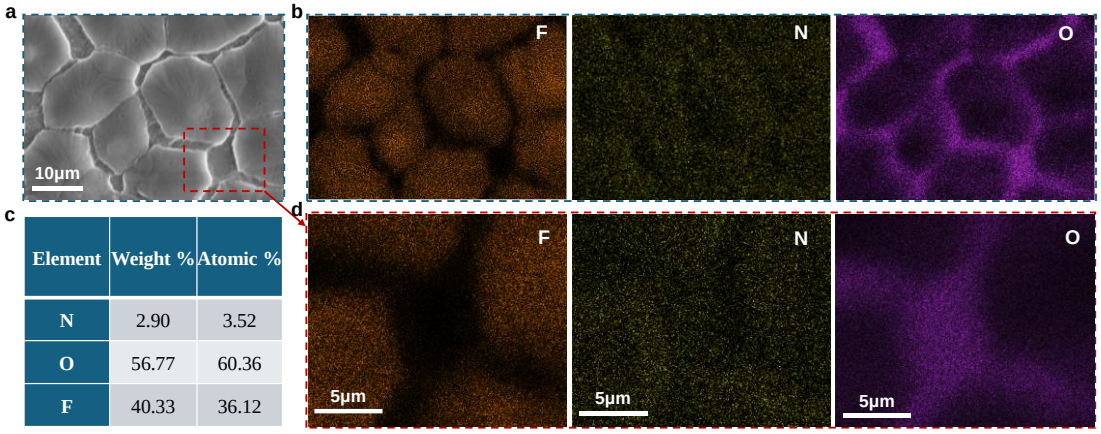

Element	Weight %	Atomic %
N	2.90	3.52
O	56.77	60.36
F	40.33	36.12

Supplementary Fig. 6. **Characterization of dry-IHCE**. a, b, SEM images (a) and corresponding electron energy dispersive X-ray spectroscopy mapping (b) of dry-IHCE. c, Elemental ratio of dry-IHCE. d, Enlarged electron energy dispersive X-ray spectroscopy mapping of the region highlighted by the red dashed box in (a).

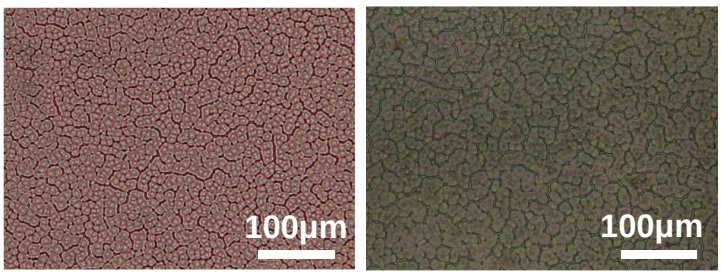

Supplementary Fig. 7. Polarizing optical microscopy images of dry-IHCE (left: bright-field, right: dark-field).

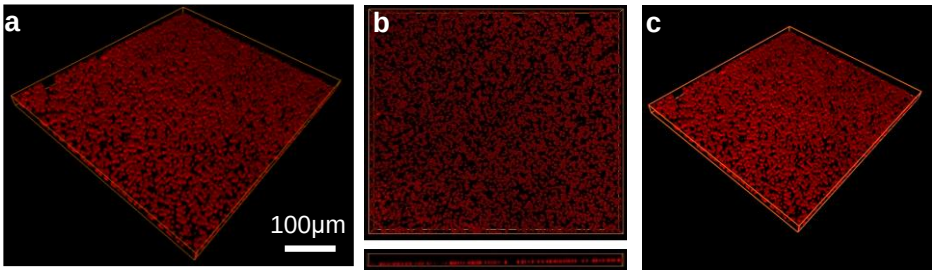

Supplementary Fig. 8. **3D laser scanning confocal microscope (LSCM)**. a-c, Top-view (a) and cross-sectional (b) LSCM images, and 3D dynamic demonstration (c) of PVDF-HFP (red phase) in dry-IHCE.

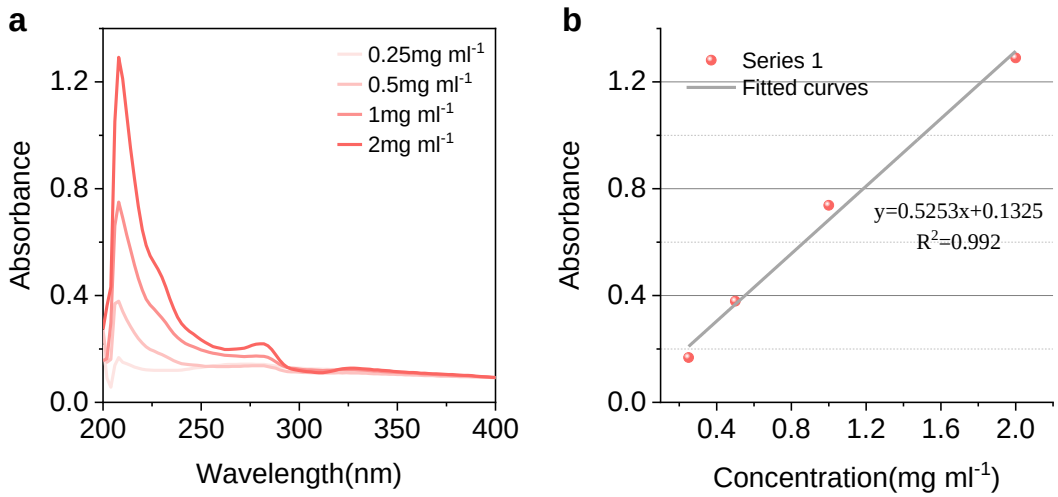

Supplementary Fig. 9. **Establishment of calibration curve for LiTFSI-DME solutions**. a, Ultraviolet-visible (UV-Vis) spectra of LiTFSI-DME solutions at various mass concentrations. b, Corresponding calibration curve for LiTFSI concentration.

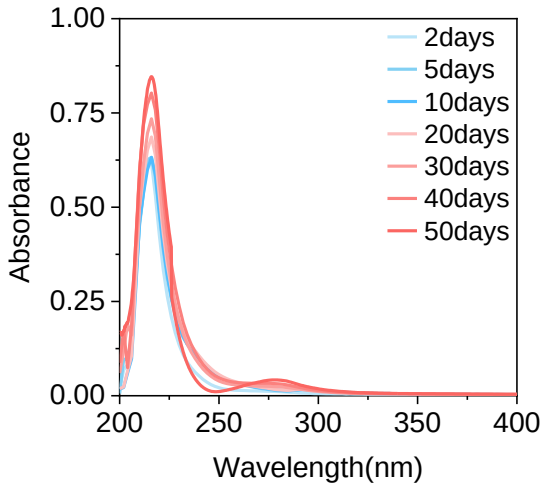

Supplementary Fig. 10. **Quantitative monitoring of LiTFSI dissolution behavior**. UV-Vis spectroscopy of LiTFSI dissolution from IHCE in DME immersion solution over time.

Supplementary Note 4:

To establish the calibration line, solutions of LiTFSI in DME with varying mass concentrations were prepared, and their UV absorption spectra were recorded at 200-400 nm (Supplementary Fig. 9a). The maximum absorption peak of the LiTFSI solutions, located at around 210 nm (belongs to the n→π* transition of -SO_2 in the LiTFSI), was selected for the linear fitting. The resulting calibration curve is shown in Supplementary Fig. 9b. The linear regression yielded an R^2 value of 0.992, indicating an excellent fit. This linear relationship serves as the standard curve, correlating the concentration of LiTFSI with its corresponding absorption intensity.

To prevent potential adsorption of LiTFSI onto cuvette walls, we employed a parallel sampling strategy: seven identical IHCE membranes were individually immersed in 3 ml of anhydrous DME and sealed in an argon-filled glove box for 2, 5, 10, 20, 30, 40, and 50 days, respectively. The corresponding masses of each IHCE membrane were 39.99, 39.99, 39.60, 40.19, 40.93, 41.93, and 41.63 mg, respectively. Based on the synthesis protocol, the mass ratio of LiTFSI and the polymer to the total IHCE was 33.2% and 66.8%, respectively (Supplementary Table 4), allowing us to estimate the initial LiTFSI content in each membrane (Supplementary Table 5). After soaking, the concentration of dissolved LiTFSI in DME was quantified using UV absorbance and calculated via Equations (5)-(6). Then, the residual LiTFSI content of IHCE (

Supplementary Table **8**) was calculated based on Equation (7).

Standard curve equation:

$$y = 0.5253 \times x + 0.1325 \tag{5}$$

$$m_{dissolved\ LiTFSI} = x \times V_{DME} = \frac{y - 0.1325}{0.5253} \times 3 \tag{6}$$

$$\begin{aligned} C_{residual\ LiTFSI\ in\ IHCE} &= \frac{m_{residual\ LiTFSI\ in\ IHCE}}{M_{LiTFSI} \times V_{solvent\ uptake\ of\ IHCE}} \\ &= \frac{m_{LiTFSI\ in\ dry-IHCE} - m_{disssolved\ LiTFSI}}{287.09 \times \frac{m_{polymer\ in\ dry-IHCE} \times 30\%}{\rho_{DME}} \times 10^{-3}} \\ &= \frac{\left(m_{dry-IHCE} \times 0.332\right) - \left(\frac{y - 0.1325}{0.5253} \times 3\right)}{287.09 \times \frac{m_{dry-IHCE} \times 0.668 \times 30\%}{0.867} \times 10^{-3}} \end{aligned} \tag{7}$$

Where "*y*" represents the UV absorbance of the LiTFSI-DME solutions. "*x*" is the mass concentration of LiTFSI-DME solutions. "m" is the mass. "*V*" is the volume. "*ρ*" is the density of DME solvent. "*C*" indicates the molar concentration.

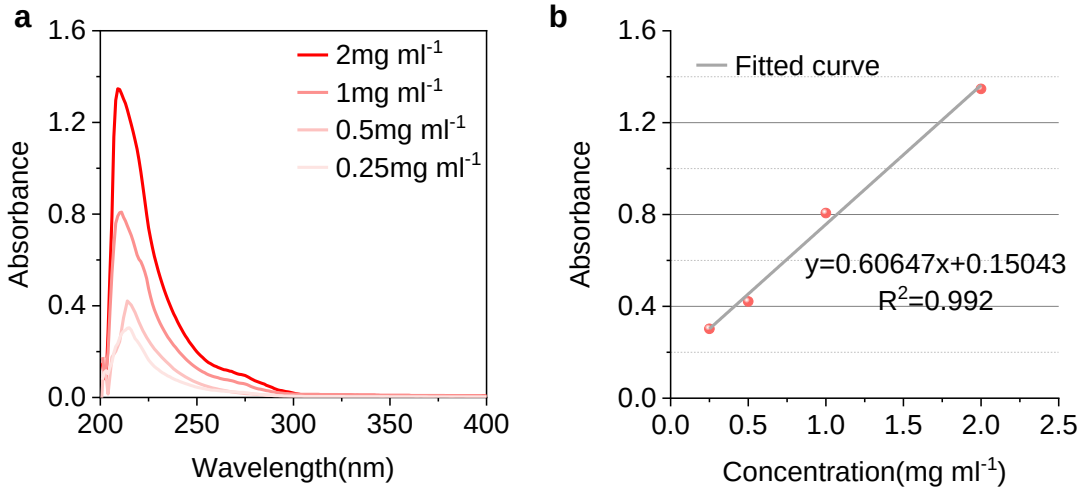

Supplementary Fig. 11. **Establishment of calibration curve of LiTFSI-FEC/DEC (1: 2, v/v) solutions**. a, UV-Vis spectra of LiTFSI-FEC/DEC solutions at various mass concentrations. b, Corresponding calibration curve for LiTFSI concentration.

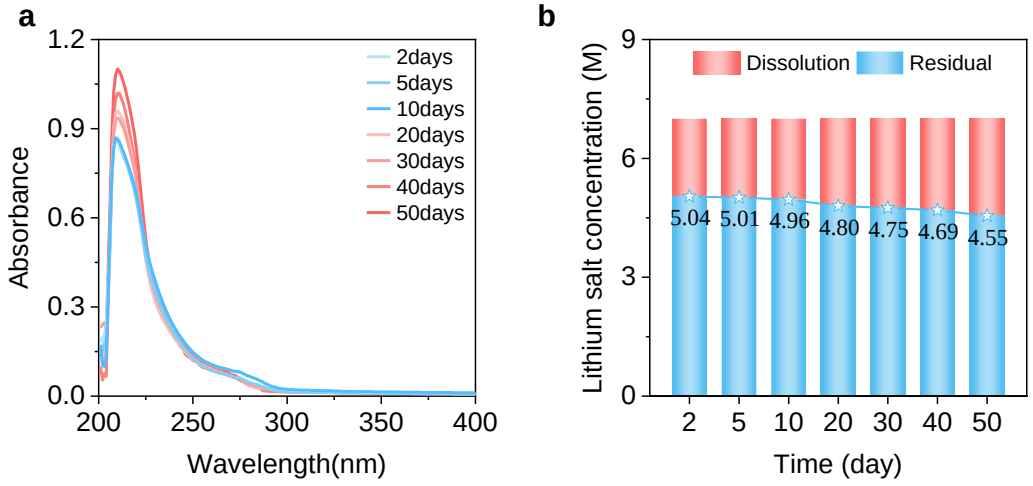

Supplementary Fig. 12. **Quantitative monitoring of LiTFSI dissolution behavior**. a, UV-Vis spectroscopy of LiTFSI dissolution from IHCE in FEC/DEC (1: 2, v/v) immersion solution over time. b, Dissolved and residual LiTFSI concentration in IHCE as a function of immersion time.

Supplementary Note 5:

To further evaluate the solvent dependence of salt-retention behavior of IHCE, we performed soaking experiments carbonate-based solvent system (FEC/DEC, 1:2 v/v).

Similar to the DME-based procedure, UV-Vis analysis was used to quantify the amount of LiTFSI retained in the IHCE membrane after immersion in the carbonate solvent. Notably, the solvent uptake of IHCE in FEC/DEC mixed solvent was measured to be ~31%, and the density of FEC/DEC (1.135 g cm^{-3}) is significantly higher than that of DME (0.867 g cm^{-3}). As a result, the same mass of IHCE membrane in FEC/DEC exhibits a higher internal electrolyte concentration of ~6.34 M, compared to 5.0 M in the DME-based system.

To quantify the amount of LiTFSI leached into FEC/DEC, a UV standard curve was first determined using the same UV-vis method described in Supplementary Note 4, by measuring the absorbance spectra of a series of LiTFSI-FEC/DEC standard solutions at ~210 nm (Supplementary Fig. 11). Then, seven identical IHCE membranes were individually immersed in 3 ml of anhydrous FEC/DEC (1: 2, v/v) and sealed in an argon-filled glove box for 2, 5, 10, 20, 30, 40, and 50 days, respectively. The corresponding masses of each IHCE membrane were 51.53, 50.72, 49.23, 48.16, 48.07, 49.76, and 50.09 mg, respectively. According to the synthesis protocol, the mass ratios of LiTFSI (33.2%) and polymer matrix (66.8%) in the total IHCE (Supplementary Table 4), and combined with the solvent uptake ratio and density, the initial LiTFSI content in each membrane was estimated.

The concentration of dissolved LiTFSI was determined based on Equations (8)-(10). The initial LiTFSI and the residual LiTFSI contents for each membrane are summarized in Supplementary Tables 7, 8. As shown in Supplementary Fig. 12, even after 50 days of immersion in FEC/DEC, the IHCE maintained a residual LiTFSI concentration >4.55 M. Compared to the initial 6.34 M concentration of LiTFSI in IHCE (FEC/DEC solvent), the daily dissolution rate was less than 0.98% during 2-50 days, demonstrating the good salt-retention ability of IHCE in carbonate-based electrolyte solvent.

These findings indicate that the salt-confinement mechanism in IHCE, driven by spatial confinement and molecular interactions, remains effective across both carbonate and ether-based electrolytes, highlighting the broad applicability of the IHCE strategy.

Standard curve equation:

$$y = 0.60647 \times x + 0.15043 \tag{8}$$

$$m_{dissolved\ LiTFSI} = x \times V_{FEC+DEC} = \frac{y - 0.15043}{0.60647} \times 3 \tag{9}$$

$$\begin{aligned} C_{residual\ LiTFSI\ in\ IHCE} &= \frac{m_{residual\ LiTFSI\ in\ IHCE}}{M_{LiTFSI} \times V_{solvent\ uptake\ of\ IHCE}} \\ &= \frac{m_{LiTFSI\ in\ dry-IHCE} - m_{disssolved\ LiTFSI}}{287.09 \times \frac{m_{polymer\ in\ dry-IHCE} \times 31\%}{\rho_{FEC+DEC}}} \\ &= \frac{\left(m_{dry-IHCE} \times 0.332\right) - \left(\frac{y - 0.15043}{0.60647} \times 3\right)}{287.09 \times \frac{m_{dry-IHCE} \times 0.668 \times 31\%}{1.135} \times 10^{-3}} \end{aligned} \tag{10}$$

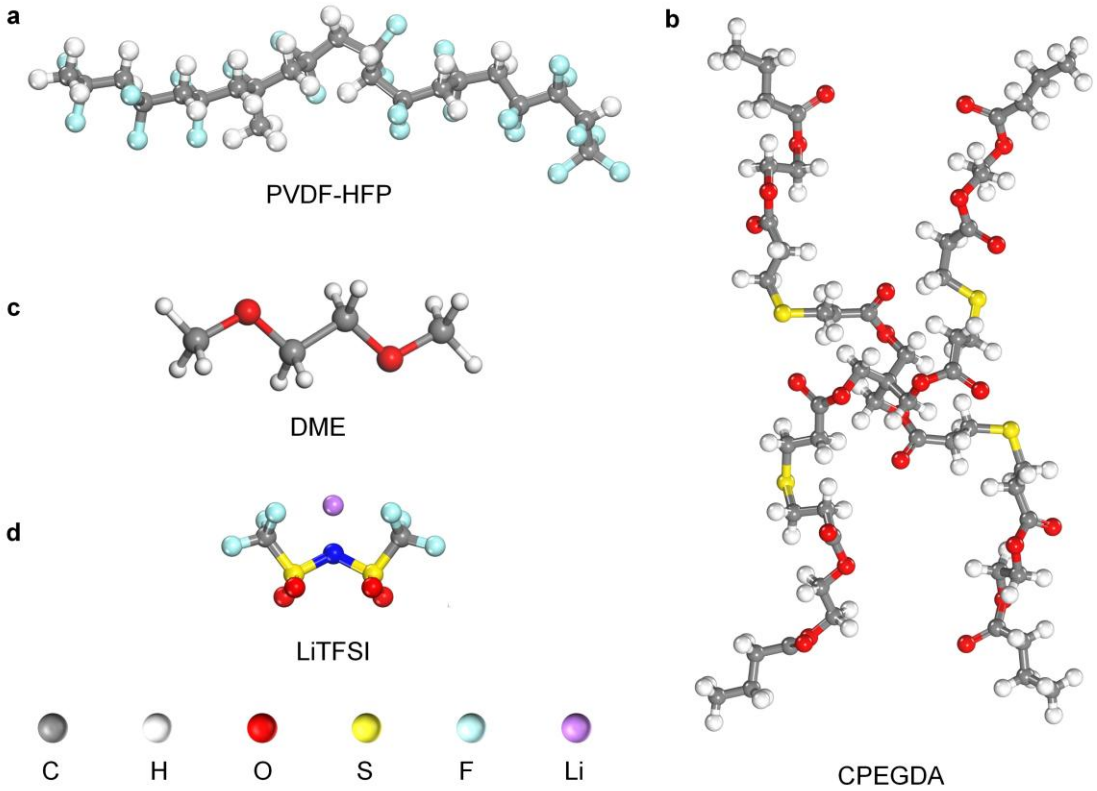

Supplementary Fig. 13. **Molecular structures and components of IHCE**. a-d, Representative structures of PVDF-HFP chains (a), CPEGDA chains (b), DME (c), and LiTFSI (d) used in simulation. Purple, lithium; red, oxygen; blue, nitrogen; ice-blue, fluorine; yellow, sulfur; grey, carbon; white, hydrogen.

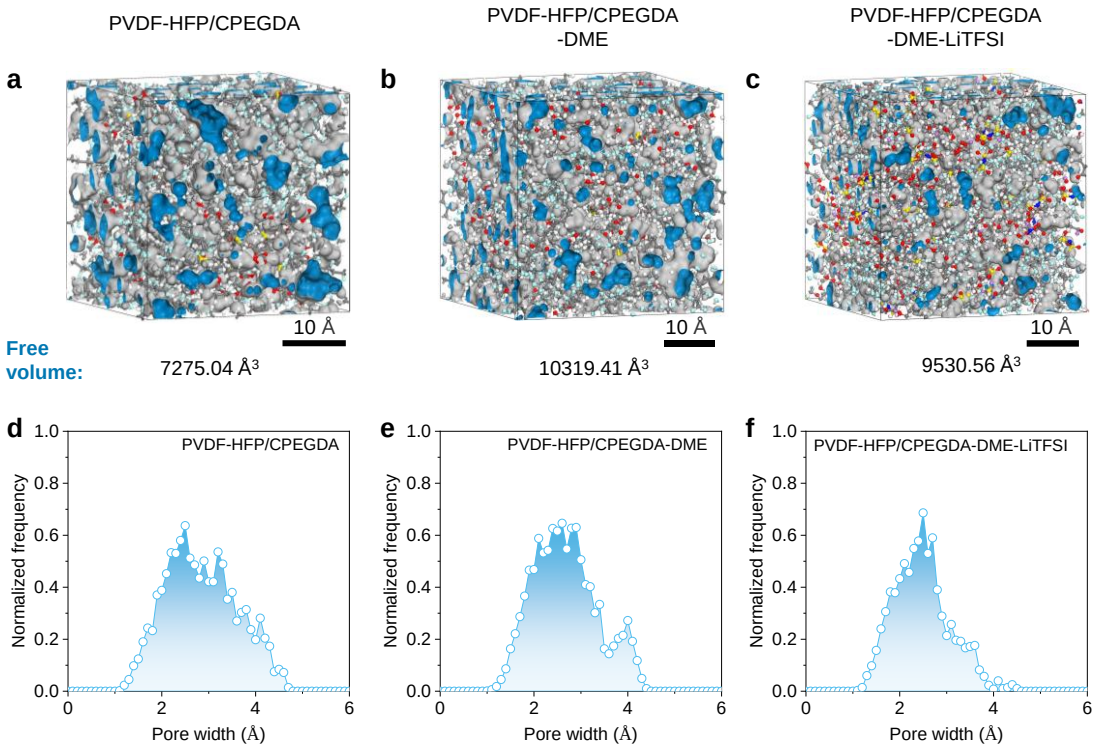

Supplementary Fig. 14. Fractional free volume (FFV) models and pore size distribution. a-c, FFV models of PVDF-HFP/CPEGDA (a), PVDF-HFP/CPEGDA-DME (b), PVDF-HFP/CPEGDA-DME-LiTFSI (c, IHCE). The grey surface indicates the van der Waals surface, and the blue surface is the Connolly surface with a probe radius of 1.3 Å. Purple, lithium; red, oxygen; blue, nitrogen; ice-blue, fluorine; yellow, sulfur; grey, carbon; white, hydrogen. d-f, Normalized pore size distributions corresponding to the models shown in (a-c).

Supplementary Note 6:

The normalized frequency is obtained from the "Derivative dist" column of the simulation results. Here, the derivative distribution is obtained by numerically differentiating the cumulative distribution G = Cumulative dist (r) with respect to the pore size bin (Δ = 0.1 Å), using the Ze0++ central difference approximation with a negative sign.

$$Derivative\_dist(r_i) \approx -\frac{C_{i+1} - C_{i-1}}{2\Delta} (i = 1, \dots, N-2) \quad (11)$$

Physically, the derivative distribution corresponds to the fractional contribution of each pore size interval to the total accessible pore volume. Numerically, it is normalized such that the integral over all pore widths equals unity.

$$\sum_i Drivative\_dist(r_i)\,\Delta \approx 1 \quad (12)$$

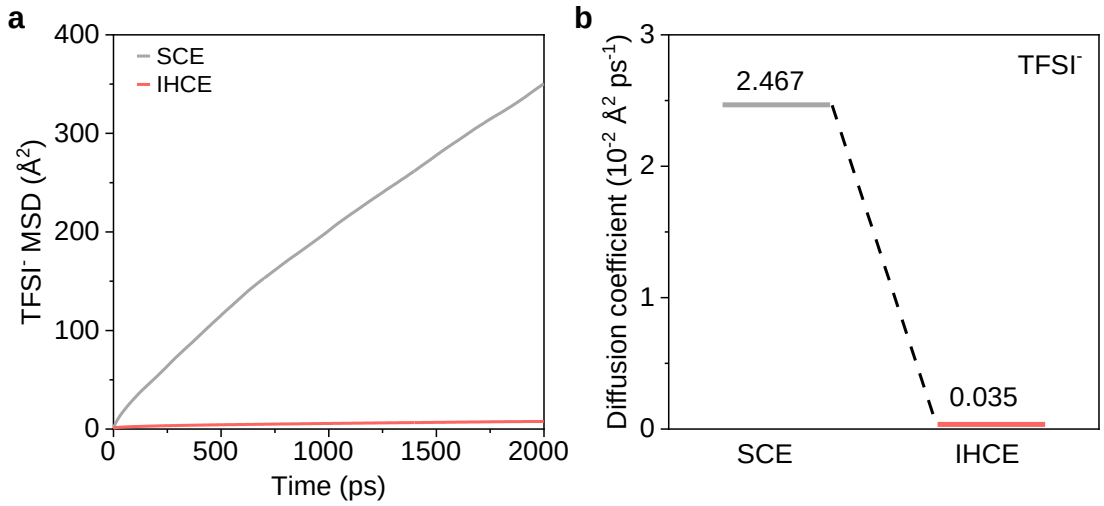

Supplementary Fig. 15. Diffusion Behavior of TFSI⁻ in SCE and IHCE. a, Calculated mean square displacement (MSD) as a function of simulation time. b, Diffusion coefficients of TFSI⁻ in SCE (1 M LiTFSI-DME) electrolyte and IHCE layer.

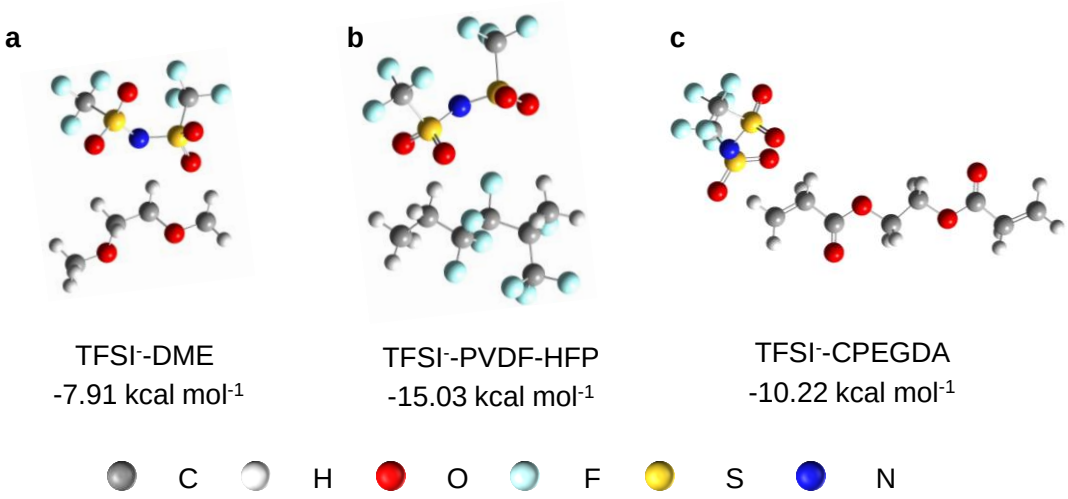

Supplementary Fig. 16. Calculated binding energies of TFSI⁻ with IHCE components. a-c, Binding energies of TFSI⁻ with DME (a), PVDF-HFP (b), and CPEGDA (c). Red, oxygen; blue, nitrogen; ice-blue, fluorine; yellow, sulfur; grey, carbon; white, hydrogen.

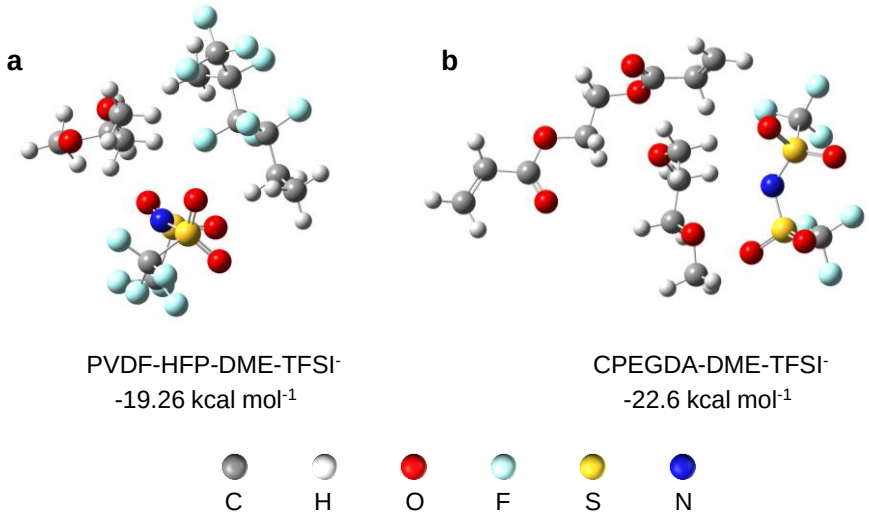

Supplementary Fig. 17. Calculated binding energies of $TFSI^-$ with polymer-solvent complexes. a, b, Binding energies of $TFSI^-$ with PVDF-HFP-DME (a) and CPEGDA-DME (b). Red, oxygen; blue, nitrogen; ice-blue, fluorine; yellow, sulfur; grey, carbon; white, hydrogen.

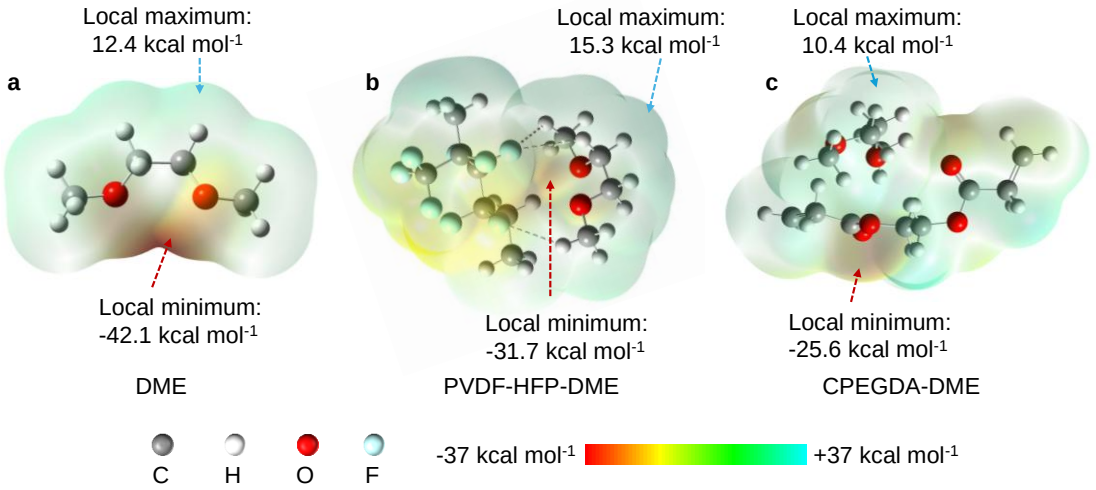

Supplementary Fig. 18. **Electrostatic potential (ESP) variations of DME upon polymer coordination**. a-c, ESP of DME (a) and after coordination with PVDF-HFP (b) or CPEGDA (c). Red, oxygen; ice-blue, fluorine; grey, carbon; white, hydrogen.

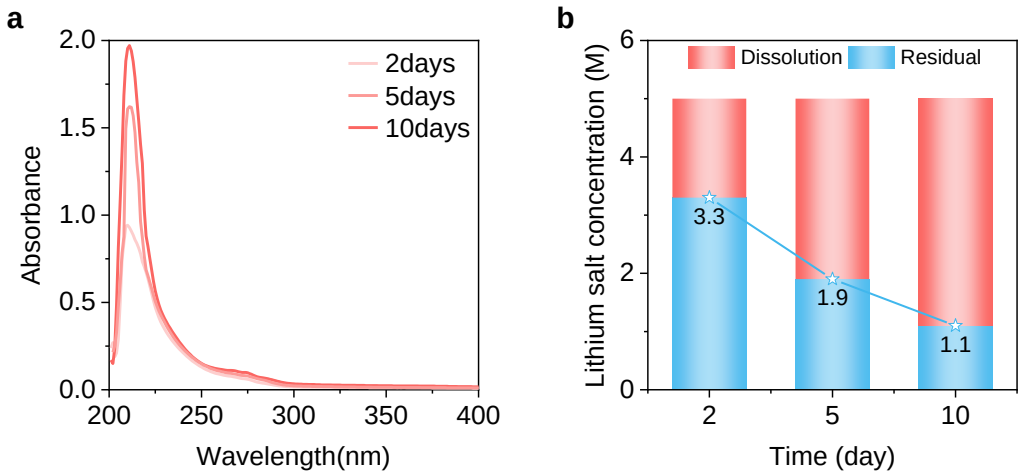

Supplementary Fig. 19. Quantitative monitoring of LiTFSI dissolution from PFO in DME over time. a, UV-Vis spectra of the DME immersion solution at different durations at 25 °C. b, Dissolved and residual LiTFSI concentration in PEO as a function of immersion time.

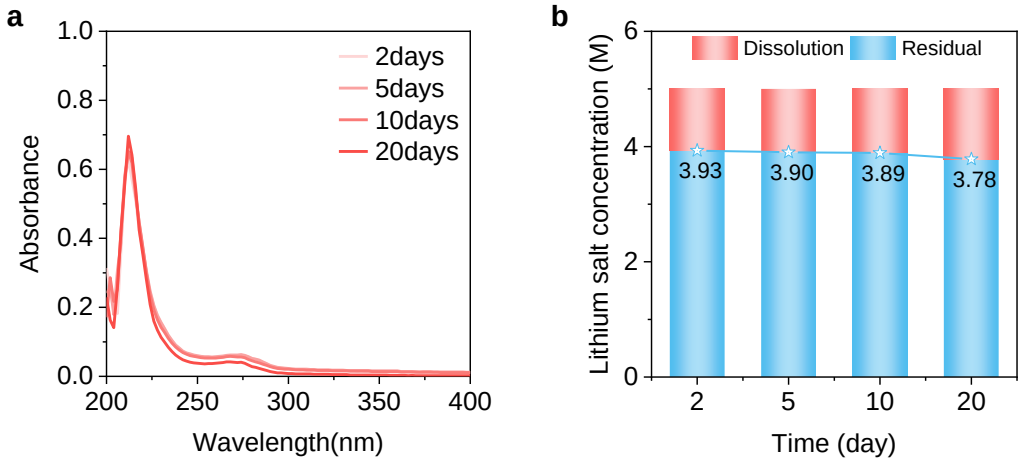

Supplementary Fig. 20. Quantitative monitoring of LiTFSI dissolution from IHCE in DME over time. a, UV-Vis spectra of the DME immersion solution at different durations at 40 °C. b, Dissolved and residual LiTFSI concentration in IHCE as a function of immersion time.

Supplementary Note 7:

To evaluate whether hydrogen bonding and ion-dipole interactions alone are sufficient to achieve similar confinement, we synthesized a comparative polymer (PFO) rich in fluorinated and ether segments but lacking the sub-nanometer-confined microstructure. The membrane was prepared via free-radical copolymerization of perfluorohexylethyl acrylate (PFHEA) and polyethylene glycol diacrylate (PEGDA). The PFHEA-to-PEGDA monomer ratio was adjusted to yield a polymer membrane

with a DME uptake of ~30 wt%, matching that of the IHCE membrane. The LiTFSI content was fixed at 50 wt% relative to total polymer mass to maintain comparable salt loading. AIBN initiator was added at 1 wt% of total monomer mass, and the polymerization was carried out at 65 °C for 12 h to ensure complete reaction. After polymerization, the resulting membrane was dried under vacuum to remove residual solvent and form a free-standing film. Using the same salt-retention testing protocol employed for IHCE, the membrane was soaked in DME, and the LiTFSI concentration was monitored over time. The mass of each PFO membrane was ~46 mg. After soaking, the concentration of dissolved LiTFSI in DME was quantified using UV absorbance and calculated via Equations (5)-(6). The residual LiTFSI content remaining in the membranes was determined using Equation (7), with results summarized in Supplementary Table 9.

We found that the residual LiTFSI concentration in the PFO membrane dropped sharply from 3.5 M (after 2 days) to 2.0 M (after 5 days), and further to 1.2 M (after 10 days) (Supplementary Fig. 19). These results suggest that hydrogen bonding and dipole interactions alone are insufficient to maintain salt confinement and the essential role of sub-nanometer-confined microstructure in achieving durable salt retention.

We also note that most polymers capable of forming sub-nanoconfined structures inherently contain nitrogen, oxygen, or hydrogen atoms, which inevitably introduce hydrogen-bonding and ion-dipole interactions with lithium salts. Thus, it is practically challenging to design a polymer that enables sub-nanometer confinement while eliminating these weak interactions for direct comparison. To further clarify the dominant factor for anion confinement, we performed temperature-dependent salt-retention experiments under an argon-filled glovebox. Considering that hydrogen bonding and ion-dipole interactions are highly sensitive to temperature, we selected 40 °C as the test condition to examine their contribution. This temperature is above typical ambient conditions (25 °C) but remains below the glass transition temperature of our polymer system, where sub-nanometer physical confinement remains structurally stable and unaffected by thermal activation. Following the same salt-

leaching protocol as at 25 °C, we soaked the IHCE membranes (~41 mg) in DME and monitored the LiTFSI concentration over time (Supplementary Fig. 20 and Supplementary **Table 10**). The residual LiTFSI content remaining in 3.93 M, 3.90 M, 3.89 M and 3.78 M after 2, 5, 10 and 20 days, respectively. These negligible changes in salt retention under moderate temperature elevation (25 to 40 °C) suggest that thermal activation does not appreciably weaken the anion retention capability. Taken together, these results provide compelling evidence that sub-nanometer physical confinement, rather than thermally sensitive weak interactions such as hydrogen bonding or ion-dipole interactions, constitutes the dominant mechanism responsible for anion retention in our IHCE system.

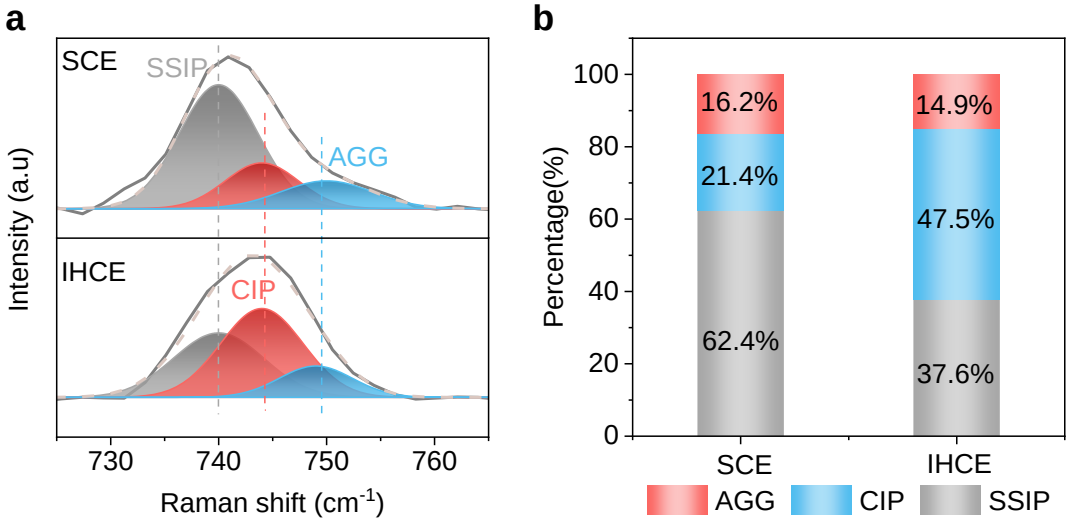

Supplementary Fig. 21. Solvation structure characterization of SCE and IHCE. a, Raman spectra of SCE and IHCE. b, Relative fractions of SSIPs, CIPs, and AGGs in SCE and IHCE derived from Raman analysis.

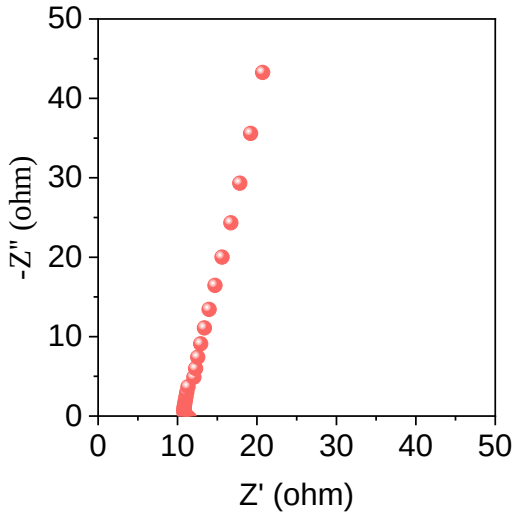

Supplementary Fig. 22. **Nyquist plots of IHCE layer at 25 °C**. R_b is determined from the intercept of the Nyquist plots with the real axis (x-axis).

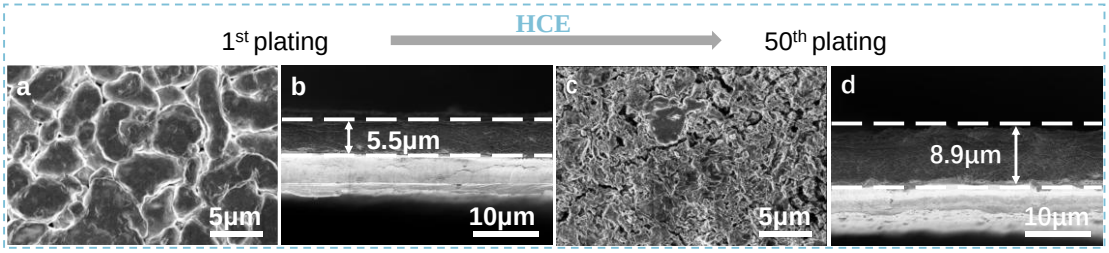

Supplementary Fig. 23. **Morphology of deposited Li on Bare Cu in HCE**. a-d, SEM images of Li deposited at 4 mA cm^{-2} with a capacity of 1 mAh cm^{-2}. Top view (a, c) and cross-sectional (b, d) SEM images of Li deposited on bare Cu in HCE after 1 cycle (a, b) and 50 cycles (c, d).

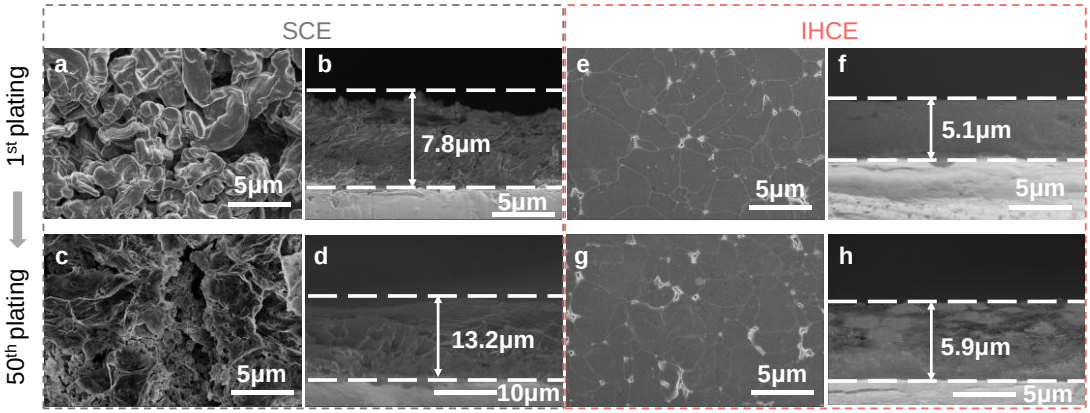

Supplementary Fig. 24. Morphology of deposited Li on Bare Cu and IHC@Cu in SCE. SEM images of Li deposited at 1 mA cm^{-2} with a capacity of 1 mAh cm^{-2}. Top view (a, c, e, g) and cross-sectional (b, d, f, h) SEM images of Li deposited on bare Cu (a-d) and IHCE@Cu (e-h) in SCE after 1 cycle (a, b, e, f) and 50 cycles (c, d, g, h).

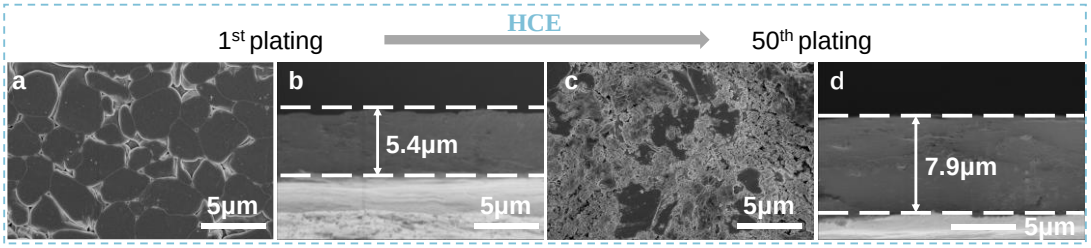

Supplementary Fig. 25. **Morphology of deposited Li on Bare Cu in HCE**. SEM images of Li deposited at 1 mA cm^{-2} with a capacity of 1 mAh cm^{-2}. Top view (a, c) and cross-sectional (b, d) SEM images of Li deposited on bare Cu in HCE after 1 cycle (a-b) and 50 cycles (c-d).

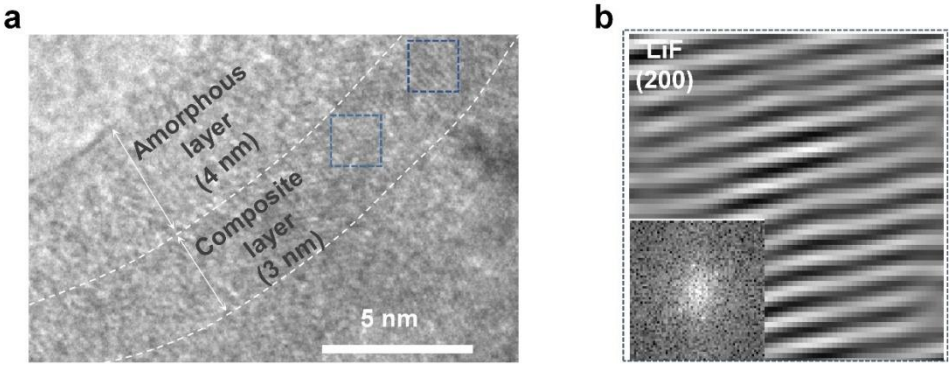

Supplementary Fig. 26. Cryo-TEM Characterization of SEI on IHCE@Cu. a, Cryo-TEM image of SEI formed on IHCE@Cu at 0.5 mA cm^{-2} with an area capacity of 0.25 mAh cm^{-2}. b, Corresponding fast Fourier transfer and high-resolution TEM images of LiF.

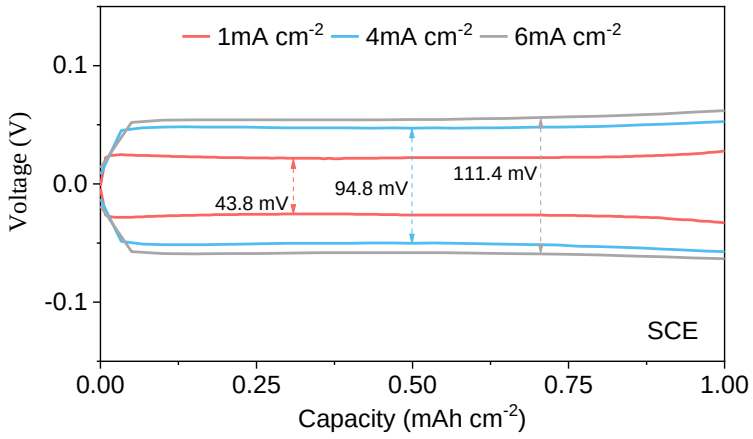

Supplementary Fig. 27. **Voltage profiles of Li||Cu half cells in SCE**. Voltage profiles of Li||Cu half cells in SCE at current densities of 1, 4, and 6 mA cm^{-2}.

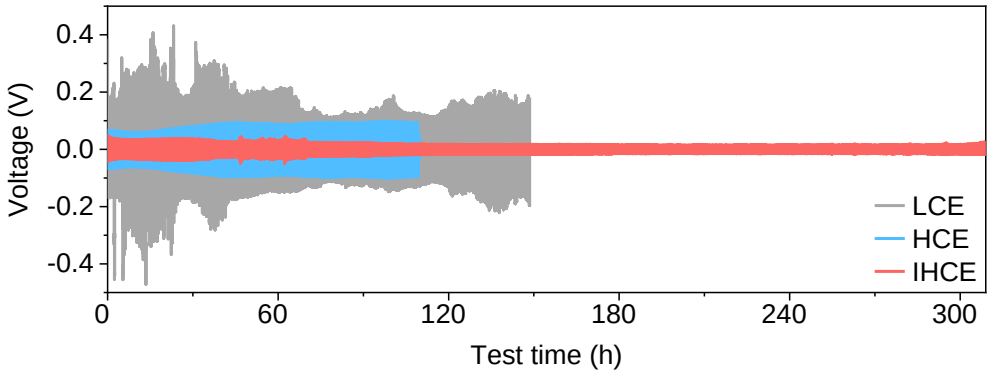

Supplementary Fig. 28. **Galvanostatic cycling of Li||Li symmetric cells**. Discharge/charge voltage profiles of Li||Li symmetric cells with SCE, HCE and IHCE at the current density of 4 mA cm^{-2} and a fixed capacity of 1 mAh cm^{-2}.

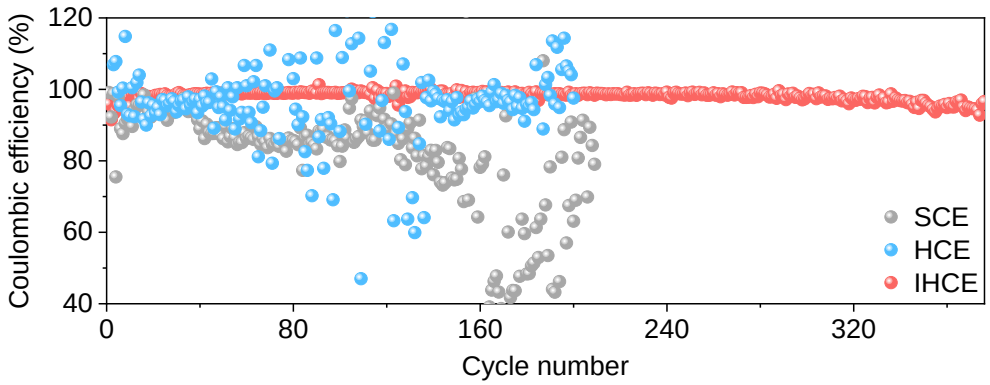

Supplementary Fig. 29. Coulombic efficiency of the Li||Cu half cells. Coulombic efficiency of the Li||Cu half cells with SCE, HCE and IHCE at the current density of 4 mA cm^{-2} with a fixed capacity of 1 mAh cm^{-2}.

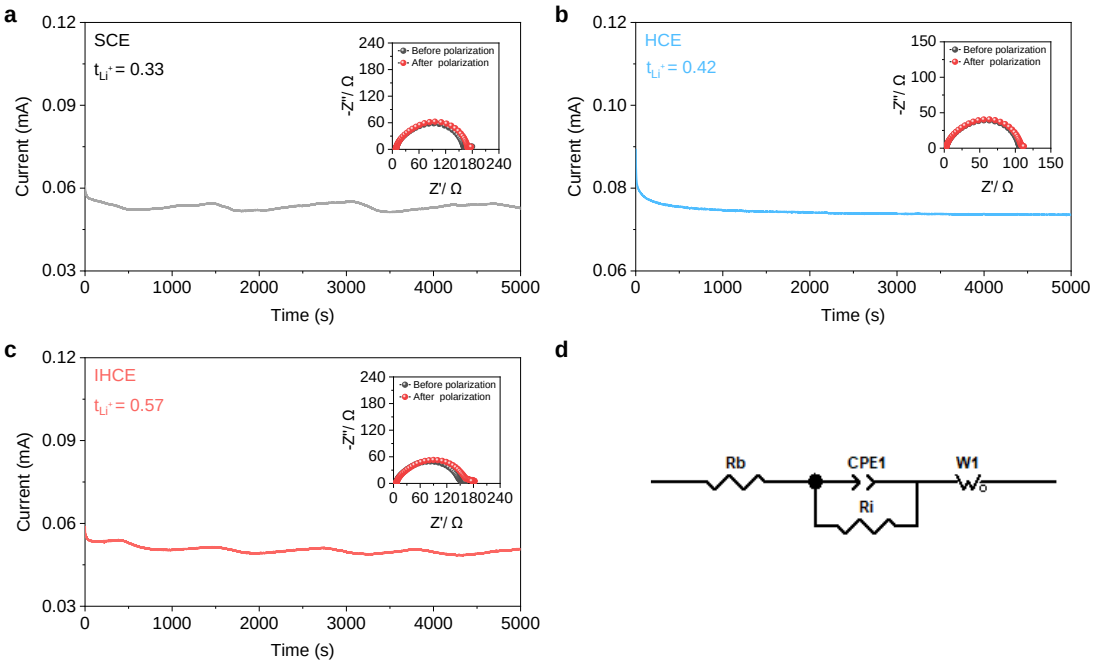

Supplementary Fig. 30. Li^+ transference number measurements. a-c, Polarization curves of SCE (a, 1 M LiFSI-DME), HCE (b, 4 M LiFSI-DME), and IHCE (c). Inset: Nyquist plots of the Li||Li symmetric cells before and after polarization. d, Equivalent circuit model (fitting values of *R* are provided in

Supplementary Table **11**)

Supplementary Note 8:

The value of Li^+ transference number ($t_{Li}{}^+$) was calculated by the Bruce-Vincent Equation (13):

$$t_{Li^+} = \frac{I_s[\Delta V - I_o(R_i^0 - R_b^0)]}{I_0[\Delta V - I_s(R_i^s - R_b^s)]} \quad (13)$$

where I_0 and I_s are the initial current and steady-state current obtained from the DC polarization measurement. The initial and steady-state values of the bulk resistances (R_b^0 and R_b^{ss}) and electrode/electrolyte interfacial resistances (R_i^0 and R_i^{ss}) were examined via EIS (from 100 kHz to 0.01Hz) before and after the potentiostatic polarization. The ΔV (10 mV) is the constant potential applied to the Li||Li symmetric cells.

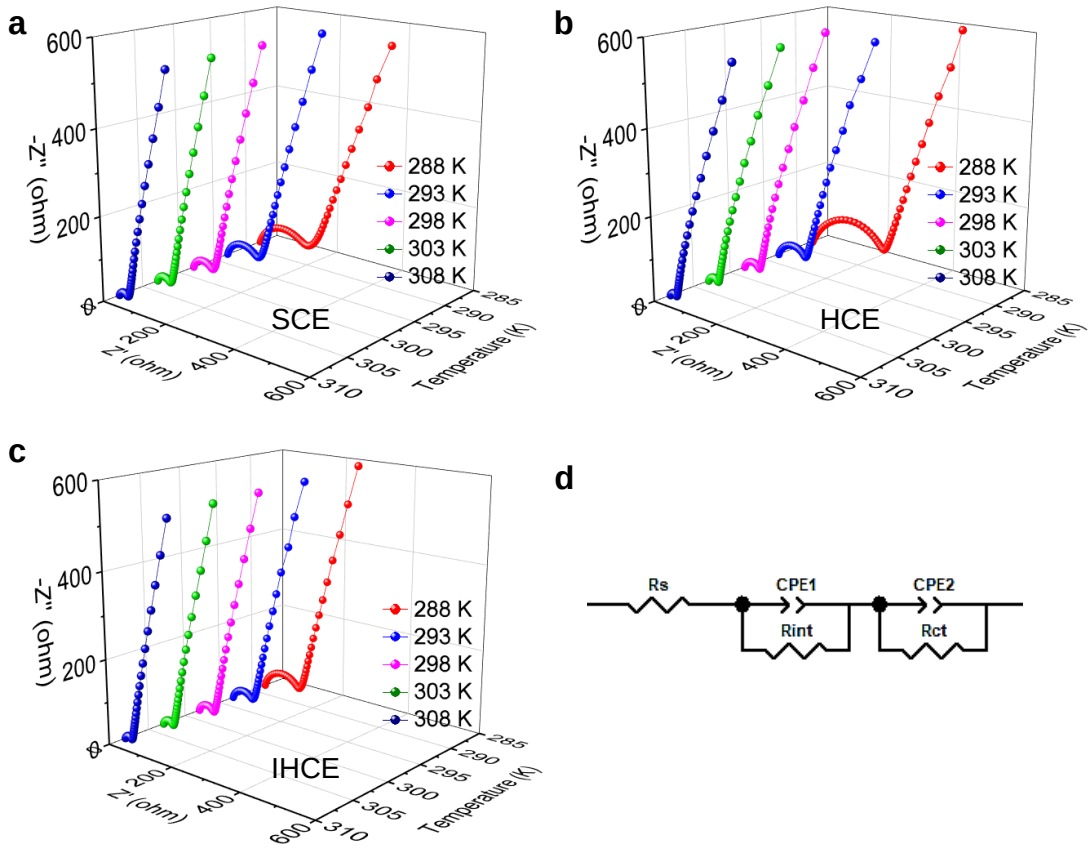

Supplementary Fig. 31. Activation energy measurments. a-c, Nyquist plots of Li||Cu asymmetric cells at temperatures ranging from 15 to 35 ℃ in SCE (a), HCE (b) and IHCE (c). d, Equivalent circuit model, where R_{int} represents the SEI resistance.

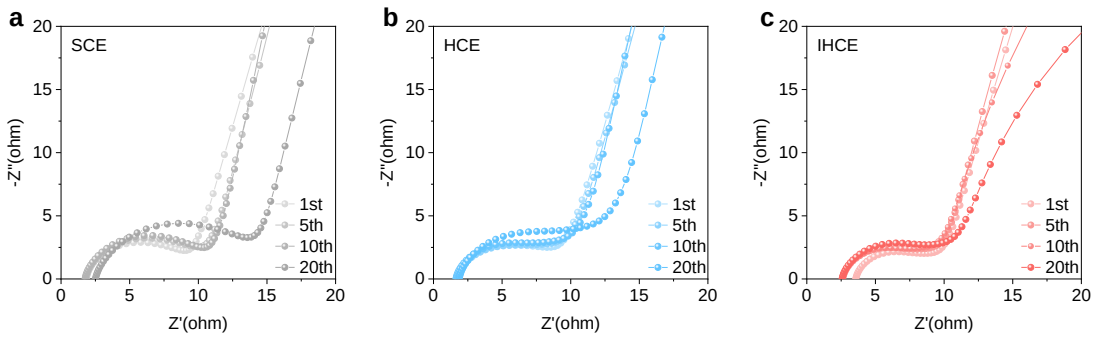

Supplementary Fig. 32. Interfacial resistance evolution during cycling. a-b, Nyquist plots of Li||Cu asymmetric cells after different cycle numbers in SCE (a), HCE (b) and IHCE (c).

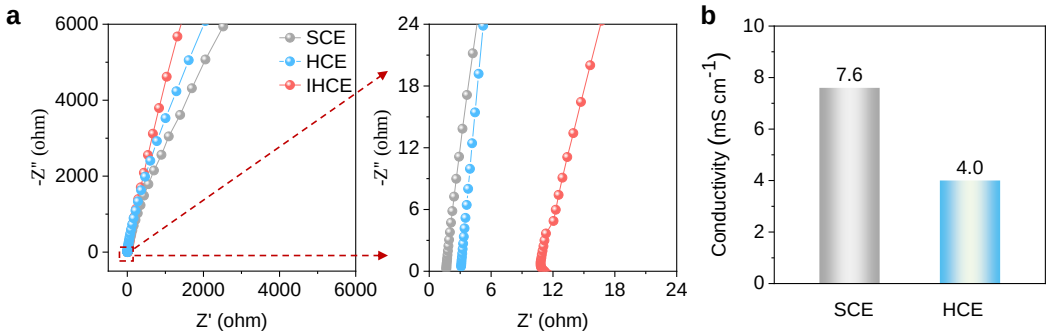

Supplementary Fig. 33. **Ionic conductivity measurements**. a, Nyquist plots of SS||SS symmetric cells with SCE, HCE and IHCE at 25 °C. b, Ionic conductivities of SCE and HCE. Conductivities were measured in the SS||SS symmetric cells using an EIS test and calculated using Equation (4). The bulk resistance (R_b) was obtained from the intercept of the Nyquist plots with the real axis (x-axis).

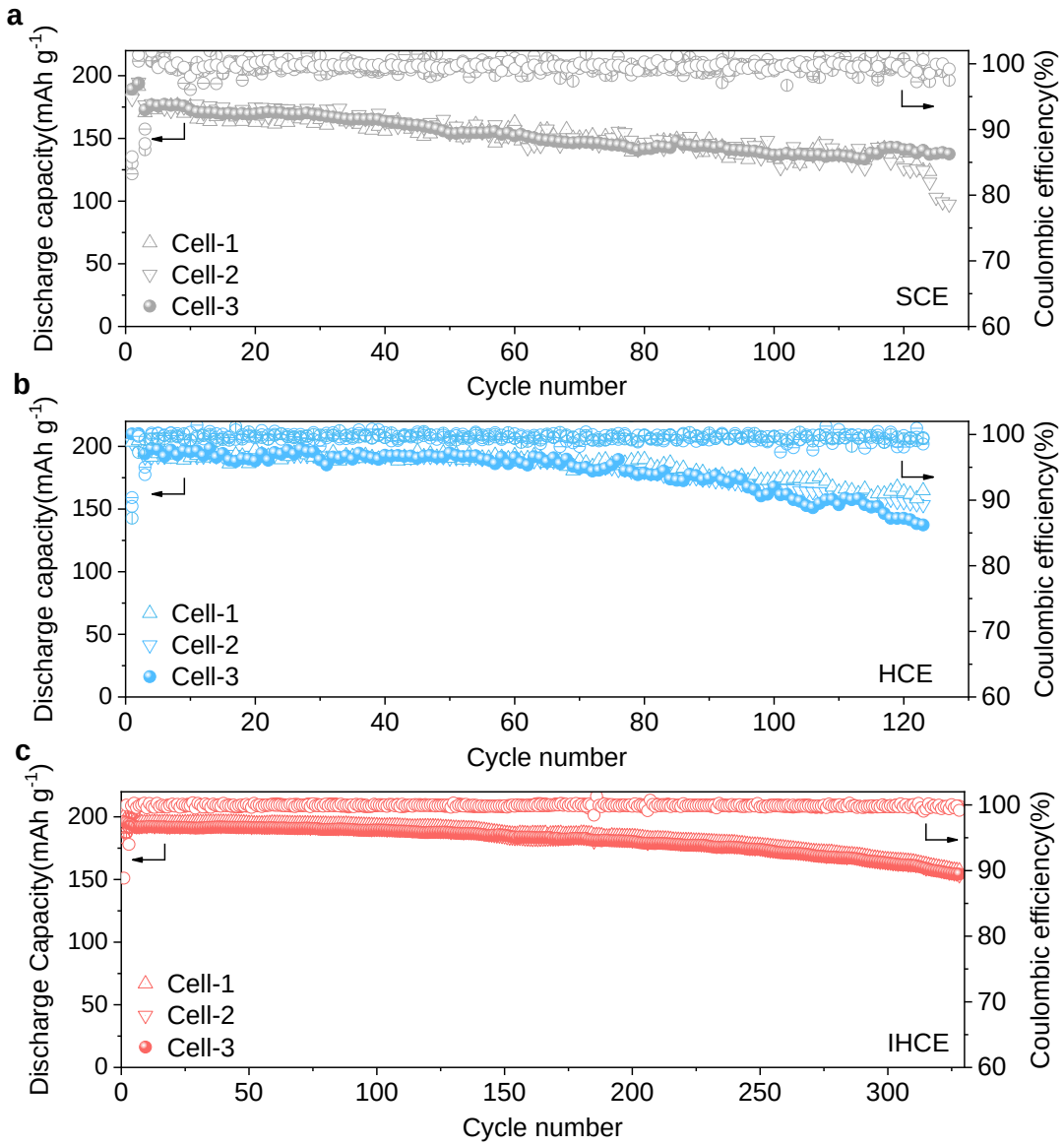

Supplementary Fig. 34. Electrochemical performance of Li||NCM811 coin cells. a-c, Long-term cycling performance of Li||NCM811 cells with SCE (a), HCE (b), and IHCE (c) at 0.5 C discharge (1 C = 180 mA g^{-1}), along with corresponding reproducibility data. The main text presents a representative cell (cell-3) consistent with the majority of the tested cells.

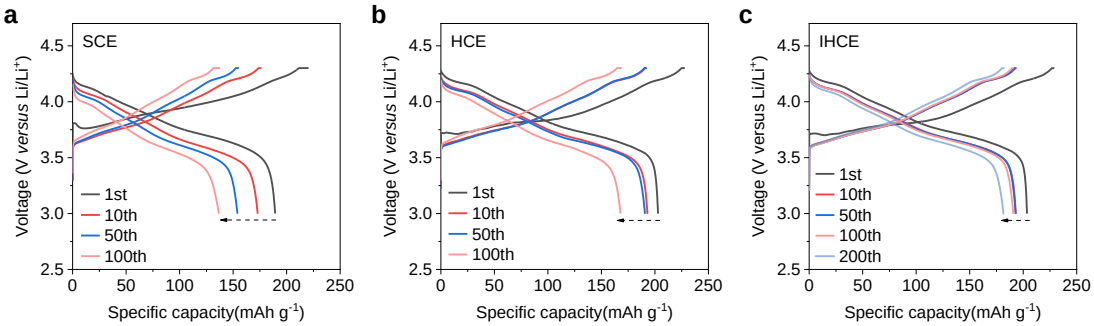

Supplementary Fig. 35. **Charge/discharge profiles of Li||NCM811 coin cells**. a-c, Charge/discharge curves of Li||NCM811 full cells (cell-3, Supplementary Fig. 34) at different cycles with SCE (a), HCE (b), and IHCE (c).

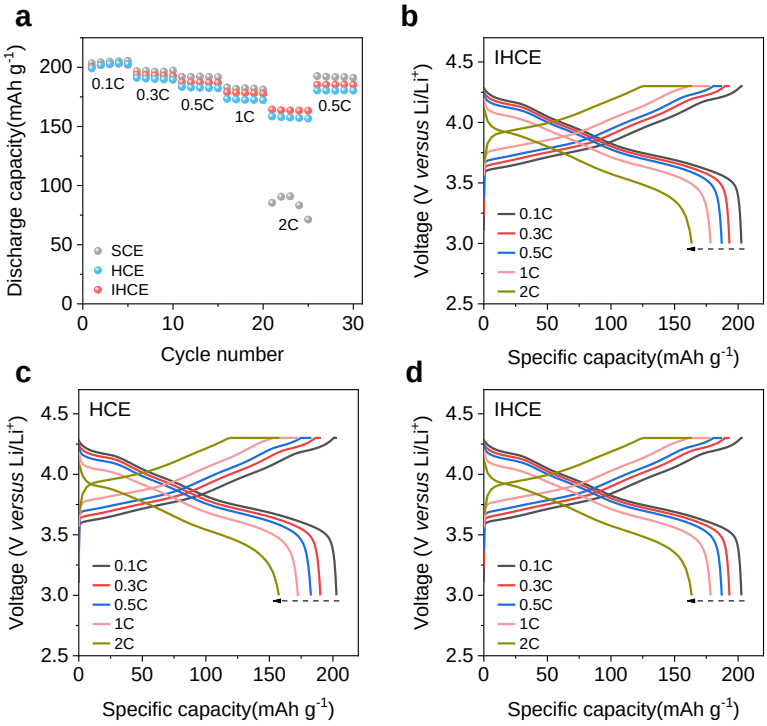

Supplementary Fig. 36. **Rate performance of the Li||NCM811 coin cells**. a, Rate performance of Li||NCM811 full cells from 0.1 C to 2 C (1 C = 180 mA g^{-1}). b-d, Charge/discharge voltage profiles of Li||NCM811 cells with IHCE (b), HCE (c), and SCE (d) at different current densities.

Supplementary Fig. 37. **The optical photograph of the IHCE@Li||NCM811 pouch cell**.

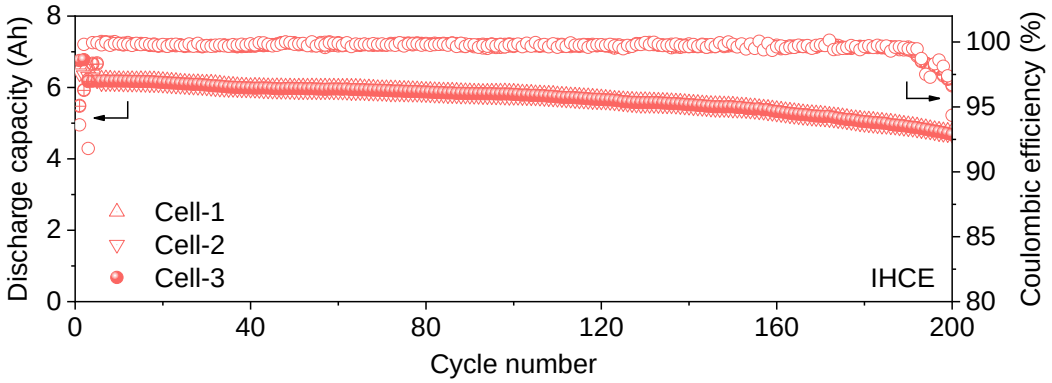

Supplementary Fig. 38. Cycling performance of IHCE@Li||NCM811 pouch cells. Cycling performance of 506 Wh kg^{-1} IHCE@Li||NCM811 pouch cells at 0.5 C discharge, along with reproducibility data. The main text presents a representative cell (cell-3) consistent with the majority of the tested cells.

Supplementary Table 1. Surface tension of individual materials, solubility parameter and Flory-Huggins interaction parameter (χ).

Materials	Surface tension (mN m^{-1})	Solubility parameter ($MPa^{1/2}$)	χ
PVDF-HFP	25.19	23.11	6.5 k
CPEGDA	31.82	20.56	

Supplementary Table 2. The detailed parameters for the calculation of ionic conductivities.

Polymer membrane	L (cm)	R_b (Ω)	S (cm^2)	σ (S cm^{-1})
PVDF-HFP_2/$CPEGDA_4$	0.028	96	2	1.46×10^{-5}
PVDF-HFP_4/$CPEGDA_6$	0.03	824	2	1.82×10^{-5}
PVDF-HFP_6/$CPEGDA_4$	0.03	840	2	1.79×10^{-5}
PVDF-HFP_8/$CPEGDA_2$	0.027	966	2	1.40×10^{-5}
IHCE (with DME)	0.025	11.2	2	1.12×10^{-3}

The fitting error of R_b is 0.311%.

Supplementary Table 3. The solvent uptake of different polymer blends.

Polymer membranes	Initial weight (m_0, mg)	Final weight (m_1, mg)	Average solvent uptake (ω)
PVDF-HFP	144; 139; 148	183; 170; 179	20 wt%
Dry-IHCE	137; 146; 136	178; 185; 181	30 wt%

Supplementary Note 9:

The solvent uptake was calculated based on the weight ratio of DME in different polymer blends. First, the initial weight of dried polymer films was weighed and recorded as m_0. Then, the polymer films were immersed in the electrolyte solvent for 12 h. After soaking, remove the polymer films and wipe off the residual liquid on their surface. Subsequently, the final weight of the corresponding films was weighed and recorded as m_1. Repeat each set of data three times and calculate the average value. The solvent uptake (ω) of the polymer films can be calculated using Equation (14):

$$\boldsymbol{\omega} = \frac{m_1 - m_0}{m_0} \times 100\% \quad (14)$$

Supplementary Table 4. Parameters of synthesized IHCE

Components	PVDF-HFP	LiTFSI	PEGDA	4-SH
Mass (g)	0.74	0.46	0.15	0.035
Total mass of polymer matrix (g)	0.925			
Total mass of dry-IHCE (g)	1.385			
Ratio of LiTFSI in dry-IHCE (%)	33.2			
Ratio of polymer in dry-IHCE (%)	66.8			

Supplementary Table 5. Usage of DME and dry-IHCE for UV experiments

Time (day)	Usage of DME (ml)	Soaked dry-IHCE (mg)	LiTFSI content in dry-IHCE (mg)
2	3	39.99	13.28
5	3	39.99	13.28
10	3	39.60	13.15
20	3	40.19	13.35
30	3	40.93	13.60
40	3	41.93	13.93
50	3	41.63	13.83

Supplementary Table 6. Parameters of UV experiments in DME.

Time (day)	UV absorbance (y)	LiTFSI in DME		Residual LiTFSI in IHCE	
		Concentration (x, mg ml^{-1})	Mass (mg)	Mass (mg)	Concentration (M)
2	0.623	0.934	2.802	10.48	3.95
5	0.632	0.952	2.855	10.43	3.93
10	0.632	0.951	2.853	10.30	3.92
20	0.686	1.054	3.162	10.18	3.82
30	0.735	1.146	3.438	10.16	3.74
40	0.803	1.276	3.829	10.10	3.63
50	0.846	1.359	4.078	9.75	3.53

Supplementary Table 7. Usage of FEC/DEC mixed solvent and dry-IHCE for UV experiments.

Time (day)	Usage of FEC/DEC (ml)	Soaked dry-IHCE (mg)	Initial LiTFSI content in dry-IHCE (mg)
2	3	51.53	17.11
5	3	50.72	16.85
10	3	49.23	16.35
20	3	48.16	16.00
30	3	48.07	15.97
40	3	49.76	16.53
50	3	50.09	16.64

Supplementary Table 8. Parameters of UV experiments in FEC/DEC.

Time (day)	UV absorbance (y)	LiTFSI in DME		Residual LiTFSI in IHCE	
		Concentration (x, mg ml^{-1})	Mass (mg)	Mass (mg)	Concentration (M)
2	0.860	1.170	3.510	13.60	5.04
5	0.865	1.178	3.535	13.31	5.01
10	0.870	1.186	3.559	12.79	4.96
20	0.936	1.295	3.886	12.11	4.8
30	0.960	1.335	4.005	11.96	4.75
40	1.020	1.434	4.301	12.22	4.69
50	1.100	1.566	4.697	11.94	4.55

Supplementary Table 9. Parameters of UV experiments of PFO.

Time (day)	UV absorbance (y)	LiTFSI in DME		Residual LiTFSI in PFO	
		Concentration (x, mg ml^{-1})	Mass (mg)	Mass (mg)	Concentration (M)
2	0.942	1.541	4.623	10.743	3.5
5	1.732	3.045	9.135	6.078	2.0
10	2.201	3.936	11.808	3.730	1.2

Supplementary Table 10. Parameters of UV experiments of IHCE at 40 ºC.

Time (day)	UV absorbance (y)	LiTFSI in DME		Residual LiTFSI in IHCE	
		Concentration (x, mg ml^{-1})	Mass (mg)	Mass (mg)	Concentration (M)
2	0.632	1.07	2.85	10.42	3.93
5	0.645	1.10	2.93	10.32	3.90
10	0.652	1.11	2.97	10.34	3.89
20	0.696	1.22	3.22	9.92	3.78

Supplementary Table 11. Detailed parameters for calculating the Li^+ transference number in SCE, HCE and IHCE.

System	R_b^0	R_i^0	R_b^{ss}	R_i^{ss}	I^o	I^{ss}	t_{Li}^+
LCE	7.904	162.7	8.018	170.7	0.061	0.053	0.33
HCE	2.504	110.5	2.506	110.1	0.088	0.075	0.42
IHCE	5.334	151.2	6.151	162.2	0.059	0.051	0.57

The fitting error of R is 1.2±0.3 %.

Supplementary Table 12. Detailed parameters used for calculating the activation energy of Li^+ transport across the SEI in SCE, HCE, and IHCE.

System	T (K)	1000/T	R_{SEI} (Ω)	Ln (T/R_{SEI})
SCE	288	3.47	31.09	2.226
	293	3.41	18.56	2.759
	298	3.36	12.76	3.151
	303	3.30	9.00	3.516
	308	3.26	6.85	3.807
HCE	288	3.47	156.6	0.609
	293	3.41	65.05	1.505
	298	3.36	35.18	2.137
	303	3.30	24.65	2.509
	308	3.26	16.41	2.932
IHCE	288	3.47	116.6	1.135
	293	3.41	65.98	1.491
	298	3.36	48.43	1.816
	303	3.30	32.57	2.230
	308	3.26	21.99	2.639

The fitting error of R_{SEI} is 0.284%.

Supplementary Table 13. Detailed parameters for calculating the ionic conductivities of SCE, HCE and IHCE.

System	L (μm)	R_b (Ω)	S (cm^2)	σ (S cm^{-1})
LCE	25	1.6	2	7.6
HCE	25	3.1	2	4.0
IHCE	25	11.2	2	1.1

R_b is determined from the intercept of the Nyquist plots with the real axis (x-axis).

Supplementary Table 14. Comparison of Li-metal coin-type full cells in previous reports and this work (criteria: area capacity ≥3 mAh cm^{-2} and capacity retention ≥80%).

Strategy	Cathode	Cathode loading (mAh cm^{-2})	N/P ratio	Cycling condition	Cycle number	Reference
UCLN	NCM811	3	2.96	0.2 C charge/discharge	50	1
PR-PAA	$LiFePO_4$	3	-	0.5 C charge/discharge	100	2
TESM	$LiFePO_4$	3	3.3	1 C charge/discharge	160	3
F-/N-containing SEI	NCM523	3.14	1.59	0.4 C charge/discharge	200	4
P(SF-DOL)	NCM523	3.4	1.9	-	200	5
PVDF–PAN	NCM811	4	2.4	0.25 C charge/discharge	150	6
CMP	NCM811	4	2.5	0.3 C charge/0.5 C discharge	160	7
PBM	NCM811	4	1.75	0.1 C charge/0.5 C discharge	220	8
IHCE	NCM811	4	1.25	0.1 C charge/0.5 C discharge	328	This work

Supplementary Table 15. The detailed parameters of 6.8 Ah-type IHCE@Li||NCM811 pouch cell.

Cell component	Cell parameters	Value
Cathode	Materials	NCM811
	Number	12
	Active material loading (%)	95.5
	Area weight (each side, mg cm^{-2})	30
	Area capacity (each side, mAh cm^{-2})	6.6
	Electrode length (mm)	82
	Electrode width (mm)	60
	NCM811 Weight (g)	33.26
	Al foil weight (g)	1.74
	NCM811 and Al foil weight (g)	35.0
Anode	Materials	IHCE@Li
	Number	13
	Li thickness (μm)	100
	Area capacity (mAh cm^{-2})	10
	N/P ratio	1.51
	Weight (g)	3.57
Electrolyte	E/C ratio (g Ah^{-1})	1.29
	Weight (g)	8.77
Separator	Weight (g)	1.6
Package and lugs	Weight (g)	2.1
Pouch cell	Mid-value voltage (V)	3.8
	Capacity (Ah)	6.8
	Total weight (g)	51.04
	Energy density (Wh kg^{-1})	506

Supplementary Note 10:

The precise Energy density was calculated using Equation (15):

$$Specific\ energy\ density\ (Wh\ kg^{-1}) = \frac{Discharge\ capacity\ (Ah) \times Mid-value\ voltage\ (V)}{Total\ weight\ (kg)} \quad (15)$$

Supplementary Table 16. Comparison data regarding pouch-type LMBs with high-energy-density over 400 Wh kg^{-1}.

Energy density (Wh kg^{-1})	Cathode	Cathode loading (mAh cm^{-2})	Li thickness (μm)	N/P ratio	Charge/ discharge rate	Capacity retention	Reference
403.0	NMC83	5.88	40	0.65	0.1 C	87.6% after 100 cycles	9
406.8	NCM811	3.83	50	1.34	0.3/0.5 C	81.5% after 65 cycles	7
413.0	NCM811	3.66	50	2.7	0.2/0.6 C	90% after 120 cycles	10
418.7	NCM811	5.7	100	1.75	0.1/0.5 C	99.2% after 70 cycles	8
425.7	NCM811	5.77	100	1.73	0.1/0.5 C	86.15% after 140 cycles	11
426.0	NCM811	4	40	2	0.2/2 C	90% after 200 cycles	12
430.4	NCM811	5.6	50	1.79	0.1/0.2 C	95% after 173 cycles	13
437.0	NCM811	3.7	50	2.7	0.2/0.3 C	95.4% after 60 cycles	14
440.0	NCM811	5.6	50	1.8	0.1/0.2 C	91.7% after 140 cycles	15
505.9	NCM811	4.2	60	1.5	0.1/0.1 C	91% after 130 cycles	16
506	NCM811	6.6	100	1.51	0.1/0.5 C	75.8% after 200 cycles	This work

Supplementary Table 17. The detailed supplier information for the electrode and cell components.

NCM811 powder	Li foil	Electrolyte components	Separator	Al foil
Xian Safty Energy Technology Co., Ltd	China Energy Lithium Co., Ltd	Suzhou Dodo Chem Co., Ltd	Shenzhen Numi Technology Co., Ltd	Shenzhen Shuanghai Trading Co., Ltd.

Supplementary Table 18. Raw materials usage and cost for IHCE synthesis.

Component	PVDF-HFP	LiTFSI	PEGDA	4-SH	AIBN	DMF
Mass (g)	0.74	0.46	0.15	0.035	0.0018	8.34
Density (g cm^{-3})	-	-	1.12	1.288	-	0.948
Unit-price (\$ g^{-1})	1.35	2.18	0.13	0.24	1.09	0.10
Cost (\$)	1.00	1.00	0.02	0.01	1.4×10^{-3}	0.82
Synthesized IHCE	Total mass (g)		9.73			
	Total cost (\$)		2.86			
	Unit-price (\$ g^{-1})		0.29			

Costs were estimated based on reagent prices from Shanghai Macklin Biochemical Co., Ltd (PVDF-HFP), Shanghai Aladdin Biochemical Technology Co., Ltd (PEGDA, AIBN, THF and DMF), Shanghai Myriad Chemical Technology Co., Ltd (4-SH) and Suzhou Dodo Chem Co., Ltd (LiTFSI). The costs could be further reduced if large-scale products are purchased directly from chemical manufacturers.

Supplementary Table 19. Usage and cost breakdown of the IHCE coating solution.

Component	Synthesized IHCE	THF	IHCE coating solution
Mass ratio	1	500	501
Density (g cm^{-3})	-	0.889	~0.889
Unit-price (\$ g^{-1})	0.29	0.08	0.08
LiTFSI content in IHCE coating solution (%)			9.46×10^{-3}

Supplementary Table 20. IHCE coating solution usage and cost for 6.8 Ah Li||NCM811 pouch cell.

Li electrode parameters			IHCE coating solution parameters				
Length (cm)	Width (cm)	Number	Unit-price (\$ g^{-1})	Total usage (g)	Unit-usage (g Ah^{-1})	Total cost (\$)	Unit cost (\$ Ah^{-1})
8.2	6	13	0.08	2.27	0.33	0.18	0.027

Supplementary Table 21. Lithium salt usage and cost per Ah for 6.8 Ah Li||NCM811 pouch cells using SCE, HCE and IHCE with an E/C ratio of 1.29 g Ah^{-1}.

Electrolytes		LiDFOB	$LiBF_4$	FEC	DEC
Unit-price ($ g^{-1})		2.18	2.18	1.42	0.41
SCE	Formula	0.6 M	0.4 M	1: 2, v/v	
	Usage (g Ah^{-1})	0.088	0.038	0.49	0.67
	Cost ($ Ah^{-1})	0.19	0.08	0.71	0.27
HCE	Formula	0.6 M	0.4 M	1: 2, v/v	
	Usage (g Ah^{-1})	0.33	0.095	0.37	0.49
	Cost ($ Ah^{-1})	0.72	0.21	0.52	0.20
IHCE coating solution	Unit-cost ($ Ah^{-1})	Ratio of LiTFSI (%)	Unit-usage (g Ah^{-1})	LiTFSI usage (g Ah^{-1})	LiTFSI cost ($ Ah^{-1})
	0.027	9.46×10^{-3}	0.33	3.16×10^{-5}	6.88×10^{-5}
Summary		SCE	HCE	IHCE	
	Salt usage (g Ah^{-1})	0.126	0.425	0.12603	
	Salt cost ($ Ah^{-1})	0.27	0.93	0.27007	
	Total cost ($ Ah^{-1})	1.25	1.65	1.28	

Costs are evaluated based on Suzhou Dodo Chem Co., Ltd (LiDFOB, $LiBF_4$, FEC, and DEC). If large-scale products are purchased directly from a chemical factory, the price can be lowered even further.

Supplementary Note 11:

Lithium Salt Consumption and Cost Analysis:

A detailed analysis of lithium salt consumption and associated costs was conducted based on a practical 6.8 Ah Li||NCM811 pouch cell configuration specifically designed in our study (Supplementary Table 15), with an electrolyte-to-capacity (E/C) ratio of 1.29 g Ah^{-1}.

The IHCE system comprised an IHCE coating layer and a bulk electrolyte with the

same composition as the SCE. Specifically, the IHCE coating solution was applied at a unit usage of 2 μl cm^{-2}, corresponding to ~1.78 mg cm^{-2}, based on its density of ~0.889 g cm^{-3}. Considering the electrode dimensions and double-sided coating on the Li foil, the unit usage of IHCE coating solution was ~0.33 g Ah^{-1} (Equation (16)). The solution contains 0.2 wt% synthesized IHCE in a THF diluent, with a LiTFSI content of 9.46 × 10^{-3} wt% (Equation (17)). Therefore, the IHCE layer contributes an additional but negligible amount of lithium salt: 3.16 × 10^{-5} g Ah^{-1} (Equation (18)).

$$\begin{aligned} m_{IHCE\ coating\ solution} &= 2 \times L \times W \times N \times Unit - usage \div 6.8 \\ &= 2 \times 8.2 \times 6 \times 13 \times 1.78 \div 1000 \div 6.8 = 0.33\ g\ Ah^{-1} \end{aligned} \quad (16)$$

$$\begin{aligned} \omega_{\text{LiTFSI in IHCE coating solution}} &= \frac{m_{LiTFSI\ in\ sythesized\ IHCE}}{m_{sythesized\ IHCE}} \times \frac{m_{sythesized\ IHCE}}{m_{IHCE\ coating\ solution}} \\ &= \frac{0.46}{9.73} \times 0.2\% \\ &= 9.46 \times 10^{-3}\% \end{aligned} \quad (17)$$

$$\begin{aligned} m_{LiTFSI\ in\ IHCE\ layer} &= m_{IHCE\ coating\ solution} \times \omega_{\text{LiTFSI in IHCE coating solution}} \\ &= 0.33 \times 9.46 \times 10^{-3}\% = 3.16 \times 10^{-5}\ g\ Ah^{-1} \end{aligned} \quad (18)$$

Where "ω" represents the mass ratio, "m" refers to mass, and "L, W, N" represent length, width, and number of Li foils.

For bulk electrolyte, the formulations used for HCE and SCE were 3 M LiDFOB + 2 M $LiBF_4$ in FEC/DEC (1: 2, v/v) and 0.6 M LiDFOB + 0.4 M $LiBF_4$ in FEC/DEC (1: 2, v/v), respectively. Based on Equations (19)-(22) and the experimental parameters summarized in Supplementary Tables 18-21, the total lithium salt consumption per Ah was calculated to be ~0.126 g Ah^{-1} for SCE, ~0.425 g Ah^{-1} for HCE, and ~0.126 g Ah^{-1} for IHCE (including both SCE and IHCE layers). These results demonstrate that IHCE design achieves a ~70.4 % reduction in lithium salt usage compared to HCE, while remaining nearly identical salt consumption to SCE (~0.025% increase).

$$\omega_{LiDFOB\ (LiBF_4)} = \frac{m_{LiDFOB\ (LiBF_4)}}{m_{LiDFOB} + m_{LiBF_4} + m_{FEC} + m_{DEC}} \times 100\% \quad (19)$$

$$m_{LiDFOB\ (LiBF_4)} = C_{LiDFOB\ (LiBF_4)} \times V_{FEC+DEC} \times M_{LiDFOB\ (LiBF_4)} \quad (20)$$

$$m_{FEC\ (DEC)} = \rho_{FEC\ (DEC)} \times V_{FEC\ (DEC)} \quad (21)$$

$$m_{lithium\ salt} = m_{LiDFOB} + m_{LiBF_4} \tag{22}$$

Where "ω" represents the percentage of lithium salt relative to the total mass of the electrolyte; "m" refers to mass; "C" represents the concentration of lithium salt in electrolyte; "V" refers to volume; "ρ" represents densities of the electrolyte solvents.

For cost analysis, we considered all raw materials used for IHCE coating layer and electrolyte preparation. Prices were based on commercial suppliers, as detailed in the Methods Section and Supplementary Table 17. Using Equations (23)-(25), with all relevant parameters summarized in Supplementary Tables 18-21. the calculated costs for SCE, HCE and IHCE were ~1.25 \$ Ah^{-1}, ~1.65 \$ Ah^{-1}, and ~1.28 \$ Ah^{-1}, respectively. This result demonstrates that IHCE reduces cost by ~22.4% compared to HCE, while the added cost of the IHCE interfacial layer is minimal (increased by ~2.16% relative to SCE). This cost-effectiveness, combined with the performance advantages of IHCE, highlights its potential as a practical and scalable alternative for lithium metal batteries.

$$\begin{aligned} Cost\ of\ SCE &= P_{LiDFOB} \times m_{LiDFOB} + P_{LiBF_4} \times m_{LiBF_4} \\ &\quad + P_{FEC} \times m_{FEC} + P_{DEC} \times m_{DEC} \\ &= 2.18 \times 0.09 + 2.18 \times 0.04 + 1.42 \times 0.49 + 0.41 \times 0.67 \\ &= 1.25\ \$\ Ah^{-1} \end{aligned} \tag{23}$$

$$\begin{aligned} Cost\ of\ HCE &= P_{LiDFOB} \times m_{LiDFOB} + P_{LiBF_4} \times m_{LiBF_4} \\ &\quad + P_{FEC} \times m_{FEC} + P_{DEC} \times m_{DEC} \\ &= 2.18 \times 0.33 + 2.18 \times 0.1 + 1.42 \times 0.37 + 0.41 \times 0.49 \\ &= 1.65\ \$\ Ah^{-1} \end{aligned} \tag{24}$$

$$\begin{aligned} Cost\ of\ IHCE &= cost\ of\ IHCE\ membrane + cost\ of\ SCE \\ &= P_{IHCE\ coating\ solution} \times \frac{m_{IHCE\ coating\ solution}}{6.8} + 1.25 \\ &= 0.027 + 1.25 \\ &= 1.28\ \$\ Ah^{-1} \end{aligned} \tag{25}$$

Where "p" represents the unit-price of the specific electrolyte component. "m" is the mass.

Supplementary Note 12:

For the traditional electrolyte composed of 1 M or 4 M lithium hexafluorophosphate ($LiPF_6$) in ethylene carbonate/diethyl carbonate (1: 1, v/v), the lithium salt usage was calculated using Equations (26)-(29):

$$\omega_{LiPF_6} = \frac{m_{LiPF_6}}{m_{LiPF_6} + m_{EC} + m_{DEC}} \times 100\% \quad (26)$$

$$m_{LiPF_6} = C \times V_{EC+DEC} \times M_{LiPF_6} \quad (27)$$

$$m_{EC+DEC} = \rho_{EC} \times V_{EC} + \rho_{DEC} \times V_{DEC} \quad (28)$$

"ω" represents the percentage of lithium salt relative to the total mass of the electrolyte; "m" refers to mass; "C" represents the concentration of the electrolyte (1 M or 4 M); "V" refers to volume; "ρ" represents densities of the electrolyte solvents.

The cost of the lithium salt was calculated using Equation (29):

$$\varphi_{LiPF_6} = \frac{P_{LiPF_6} \times m_{LiPF_6}}{P_{LiPF_6} \times m_{LiPF_6} + P_{EC} \times m_{EC} + P_{DEC} \times m_{DEC}} \times 100\% \quad (29)$$

"φ" represents the percentage of lithium salt cost relative to the total cost of the electrolyte. "p" represents the unit cost of the specific electrolyte components. The unit prices of $LiPF_6$, EC, and DEC are 1.805, 0.508, and 0.508 \$ g^{-1}, respectively, as collected from Suzhou Dodo Chem Co., Ltd.

The increase in LiPF6 concentration from 1 M to 4 M results in a significant rise in both lithium salt consumption and cost. Specifically, lithium salt usage jumps from 11% to 33%, while the cost escalates from 32% to 65%. This substantial increase in lithium salt usage and associated costs poses challenges to resource conservation and hinders progress toward sustainable development.

Reference

1. Jiang, G. *et al.* Robust artificial solid-electrolyte interfaces with biomimetic ionic channels for dendrite-free Li Metal Anodes. *Adv. Energy Mater.* **11**, 2003496 (2021).

2. Gao, R.-M. *et al.* Fatigue-resistant interfacial layer for safe lithium metal batteries. *Angew. Chem. Int. Ed.* **60**, 25508–25513 (2021).
3. Ju, Z. *et al.* Biomacromolecules enabled dendrite-free lithium metal battery and its origin revealed by cryo-electron microscopy. *Nat Commun* **11**, 488 (2020).
4. Cheng, X. *et al.* Electrochemically and thermally stable inorganic-rich solid electrolyte interface for robust lithium metal batteries. *Adv. Mater.* **36**, 2307370 (2024).
5. Gao, Y. *et al.* Polymer–inorganic solid–electrolyte interphase for stable lithium metal batteries under lean electrolyte conditions. *Nat. Mater.* **18**, 384–389 (2019).
6. Wang, D. *et al.* Phase-separation-induced porous lithiophilic polymer coating for high-efficiency lithium metal batteries. *Nano Lett.* **21**, 4757–4764 (2021).
7. Zhang, K. *et al.* A High-performance lithium metal battery with ion-selective nanofluidic transport in a conjugated microporous polymer protective layer. *Adv. Mater.* **33**, 2006323 (2021).
8. Zhao, P. *et al.* Constructing self-adapting electrostatic interface on lithium metal anode for stable 400 Wh kg^{-1} pouch cells. *Adv. Energy Mater.* **12**, 2200568 (2022).
9. Liu, Z. *et al*. Expansion-tolerant lithium anode with built-in LiF-rich interface for stable 400 Wh kg^{-1} lithium metal pouch cells. *ACS Materials Lett.* **4**, 1516–1522 (2022).
10. Xia, Y. *et al.* Designing an asymmetric ether-like lithium salt to enable fast-cycling high-energy lithium metal batteries. *Nat Energy* **8**, 934–945 (2023).
11. Zhang, Y. *et al.* Enabling 420 Wh kg^{-1} stable lithium-metal pouch cells by lanthanum doping. *Adv. Mater.* **35**, 2211032 (2023).
12. Zhang, G. *et al.* A monofluoride ether-based electrolyte solution for fast-charging and low-temperature non-aqueous lithium metal batteries. *Nat Commun* **14**, 1-13 (2023).
13. Zhang, Q.-K. *et al.* Reforming the uniformity of solid electrolyte interphase by nanoscale structure regulation for stable lithium metal batteries. *Angew. Chem. Int. Ed.* **135**, e202306889 (2023).

14.Zhang, S. *et al. In situ* -polymerized lithium salt as a polymer electrolyte for high-safety lithium metal batteries. *Energy Environ. Sci.* **16**, 2591–2602 (2023).

15.Zhang, Q.-K. *et al.* Homogeneous and mechanically stable solid–electrolyte interphase enabled by trioxane-modulated electrolytes for lithium metal batteries. *Nat Energy* **8**, 725–735 (2023).

16.Jie, Y. *et al.* Towards long-life 500 Wh kg^{-1} lithium metal pouch cells via compact ion-pair aggregate electrolytes. *Nat Energy* **9**, 987–998 (2024).